A cryptic sequence targets the adhesion complex scaffold ANKS4B to apical microvilli to promote enterocyte brush border assembly

Received for publication, April 7, 2020, and in revised form, June 30, 2020 Published, Papers in Press, July 6, 2020, DOI 10.1074/jbc.RA120.013790

Maura J. Graves‡, Samaneh Matoo‡, Myoung Soo Choi, Zachary A. Storad, Rawnag A. El Sheikh Idris, Brooke K. Pickles, Prashun Acharya, Paula E. Shinder, Taylen O. Arvay, and Scott W. Crawley*

From the Department of Biological Sciences, University of Toledo, Toledo, Ohio, USA

Edited by Enrique M. De La Cruz

Nutrient-transporting enterocytes interact with their luminal environment using a densely packed collection of apical microvilli known as the brush border. Assembly of the brush border is controlled by the intermicrovillar adhesion complex (IMAC), a protocadherin-based complex found at the tips of brush border microvilli that mediates adhesion between neighboring protrusions. ANKS4B is known to be an essential scaffold within the IMAC, although its functional properties have not been thoroughly characterized. We report here that ANKS4B is directed to the brush border using a noncanonical apical targeting sequence that maps to a previously unannotated region of the scaffold. When expressed on its own, this sequence targeted to microvilli in the absence of any direct interaction with the other IMAC components. Sequence analysis revealed a coiled-coil motif and a putative membrane-binding basic-hydrophobic repeat sequence within this targeting region, both of which were required for the scaffold to target and mediate brush border assembly. Size-exclusion chromatography of the isolated targeting sequence coupled with *in vitro* brush border binding assays suggests that it functions as an oligomer. We further show that the corresponding sequence found in the closest homolog of ANKS4B, the scaffold USH1G that operates in sensory epithelia as part of the Usher complex, lacks the inherent ability to target to microvilli. This study further defines the underlying mechanism of how ANKS4B targets to the apical domain of enterocytes to drive brush border assembly and identifies a point of functional divergence between the ankyrin repeat–based scaffolds found in the IMAC and Usher complex.

Intestinal enterocytes undergo an intricate morphogenic program to become specialized to mediate nutrient absorption in the gut. During terminal differentiation, each enterocyte constructs a highly ordered array of ~1000 lumen-oriented apical microvilli that are enriched in nutrient processing enzymes and transport channels (1). Collectively these microvilli form the intestinal brush border (BB), a cellular adaptation that alone is responsible for nutrient uptake in the gut. Along with nutrient absorption, BB microvilli also play an important role in barrier function in the intestine. Enterocyte microvilli are coated by a thick glycocalyx at their apical tips (2, 3) and also secrete antimicrobial vesicles into the lumen of the intestine (4, 5). Together, these structural and functional properties help ensure the integrity of host tissue against potentially harmful toxins and microbes that can be found in the gut lumen. The importance of the BB is underscored by the fact that genetic conditions or acquired infections that perturb BB structure can be life-threatening, as seen with microvillus inclusion disease (6) and the attaching/effacing microbe enterohemorrhagic *Escherichia coli* (7).

A defining feature of the BB is its exquisite organization. During BB assembly, microvilli pack together into near-perfect hexagonal arrays, which allows for their maximum number to be constructed on the apical surface of each enterocyte (1). Furthermore, the lengths of microvilli are remarkably uniform both within and across neighboring enterocytes. Investigations into the mechanism underlying the assembly of the BB led to the discovery of a protocadherin-based adhesion complex that plays a key role in promoting BB organization (8). During construction of the BB, physical adhesion between neighboring microvilli controls their ordered packing. This adhesion is mediated by a pair of protocadherins: CDHR2 (cadherin-related family member 2; also known as protocadherin-24) and CDHR5 (cadherin-related family member 5; also known as mucin-like protocadherin) (8). These protocadherins reside at the distal tips of BB microvilli and interact in *trans* via a heterophilic adhesion bond to create "intermicrovillar adhesion links" that connect neighboring microvilli to control organization. Correct targeting and function of these protocadherins require a host of cytoplasmic factors. These factors include the two scaffolding proteins USH1C (also known as Harmonin) and ANKS4B (ankyrin repeat and sterile α-motif domain containing 4B), the myosin motor protein Myo7b (Myosin-7b), and the myosin light chain CALML4 (calmodulin-like protein-4) (8–11). Altogether, these components are known as the intermicrovillar adhesion complex (IMAC).

Within the IMAC, ANKS4B forms a stable tripartite complex with USH1C and Myo7b (9, 12, 13). In both *in vitro* reconstitution assays and cell-based experiments, these three IMAC components interact to form dense condensates via liquid–liquid phase separation (14). ANKS4B is comprised of an N-terminal ankyrin-repeat domain (denoted here as $ANKR_{min}$), a central unstructured region (CEN), and a C-terminal sterile α-motif (SAM) ending in a PDZ-binding motif (PBM). ANKS4B uses its SAM–PBM domain to bind USH1C with high

This article contains supporting information.
‡These authors contributed equally to this work.
*For correspondence: Scott W. Crawley, william.crawley@utoledo.edu.

© 2020 Graves et al. Published under exclusive license by The American Society for Biochemistry and Molecular Biology, Inc.

affinity (K_d = ~4 nM), whereas its CEN domain interacts with Myo7b with moderate affinity (K_d = ~1 μM) (13). In contrast, a binding partner for the $ANKR_{min}$ domain has not been identified to date. Loss of ANKS4B has a striking effect on CACO-2_{BBE} cells, an enterocyte model system that uses the IMAC to construct a near tissue-like apical BB after a prolonged period in culture (8, 15). ANKS4B knockdown (KD) CACO-2_{BBE} cells have severely disrupted BBs that exhibit a lower density of microvilli that are both disheveled in organization and lack uniform length (9). The protein levels of the remaining IMAC components are also markedly reduced in ANKS4B KD cells, suggesting that ANKS4B plays a crucial role in stabilizing the mature adhesion complex. The closest homolog to ANKS4B is the scaffold USH1G (also known as Sans) (16). USH1G is a component of the Usher complex, an adhesion complex homologous to the IMAC that is most well-studied for its role in forming the "tip links" that connect adjacent stereocilia on the surface of mechanosensory hair cells of the inner ear (17). In addition to USH1G, the Usher complex is comprised of the adhesion molecules CDH23 (cadherin-23) and PCDH15 (protocadherin-15), the scaffold USH1C, and the motor Myo7a (Myosin-7a) (18). Loss of any component of the Usher complex results in USH1, a severe form of deaf-blindness in humans (17, 19–24). Interestingly, USH1C overlaps as a component in both the IMAC and the Usher complex. In agreement with this, USH1 patients with genetic defects in USH1C have been reported to also suffer from severe inflammatory enteropathy in addition to the typical neurosensory deficits associated with the disease (20, 25).

In this study we sought to further characterize the functional properties of ANKS4B within the IMAC. Toward this goal, we used CACO-2_{BBE} cells to perform structure–function studies and discovered that ANKS4B localizes to apical microvilli using a cryptic targeting sequence found in a previously unannotated region of the protein. Although this sequence does not display any overt homology to other known canonical structured domains, our functional analysis identified a number of conserved sequence motifs within this region of ANKS4B that were essential for apical targeting of the scaffold. Importantly, this targeting sequence localized to apical microvilli independent of a direct interaction with the other known IMAC components and was required for the function of ANKS4B in promoting BB assembly during enterocyte polarization. We further show the apical targeting ability of this sequence represents a possible point of functional divergence between the ankyrin repeat-based scaffolds that operate in the IMAC and the Usher complex. Together, these data reveal that ANKS4B exhibits characteristics that may allow it to function as the "primordial" scaffold that targets the IMAC to the apical domain of enterocytes to drive BB assembly.

Results

Apical targeting of ANKS4B correlates with BB assembly

CACO-2_{BBE} cells construct a well-ordered apical BB when allowed to polarize for extended periods in cell culture (15). During this process, microvilli assemble into organized clusters on the apical surface as a result of the adhesion activity of the IMAC (8). To gain insight into the functional properties of ANKS4B during BB assembly, we followed the expression profile of this IMAC scaffold by immunoblot analysis across a developmental time series of CACO-2_{BBE} cells. We have previously shown that all the other known IMAC components are largely absent from the early time points of CACO-2_{BBE} cell development (8, 11), with protein levels only beginning to accumulate at the onset of BB assembly (Fig. 1*A*; see CALML4 as example). In contrast, ANKS4B could be detected across all time points of our developmental time series (Fig. 1*A*). Interestingly, ANKS4B exhibited a laddered appearance by immunoblot analysis, with multiple higher-molecular-mass species being detected. The dominant band in fully polarized cells was the lowest-mass species, which migrated at an apparent molecular mass of ~52 kDa (Fig. 1*A*, *arrow*), slightly larger than the theoretical mass of 46.6 kDa for ANKS4B. After day 2, this lower-mass species rapidly increased in quantity to end up constituting ~95% of the total ANKS4B signal detected in mature cells (days 14–21). Although the nature of the higher mass species of ANKS4B remains unknown, we noted that these bands tended to collapse when samples were reheated multiple times. This may suggest that they represent oligomers of the scaffold that are partially resistant to disruption by heating and detergent.

To further explore how ANKS4B behaves during CACO-2_{BBE} differentiation, we stained for endogenous ANKS4B in CACO-2_{BBE} cells across a similar polarization time course. For this analysis, we assessed the relative enrichment of ANKS4B in the apical domain compared with the total cellular signal at each time point (Fig. 1*B*; see also Fig. S1*A* for demarcation examples). During the early stages of BB development (days 0–2), apical microvilli appeared small and did not organize into distinct clusters that would be indicative of active IMAC within these protrusions (Fig. 1*C*). In agreement with this, ANKS4B was largely absent from the apical domain at the beginning of polarization, appearing mostly as distinct puncta within the cytoplasm (Fig. 1, *B* and *C*, day 0 cells, *arrows*). We did observe discrete examples of individual cells that appeared to have more pronounced microvilli that displayed some apical targeting of ANKS4B (see *asterisk* in the zoomed panel, day 2 cells), although cells with these characteristics were relatively rare at early time points. ANKS4B became rapidly enriched in the apical BB at the first appearance of clustering of microvilli at day 4; however, targeting of the scaffold was not exclusively restricted to the distal tips of microvilli (Fig. 1*C*, day 4). Indeed, microvilli at this time point were relatively small and immature and only formed rudimentary clusters that were not well-organized. Clear targeting to the distal tips of BB microvilli typically appeared at time points of day 6 and beyond, with microvilli forming well-structured clusters that organized into various patterns as previously seen with this cell line (Fig. 1*C*, days 6–14) (8, 10).

To investigate the *in vivo* apical targeting properties of ANKS4B, we stained mouse duodenal tissue sections and imaged the scaffold across the crypt–villus axis, which allowed us to visualize the entire life cycle of enterocytes in a single tissue section (Fig. S1*B*). As a marker for BB microvilli, we used an antibody that specifically recognizes the active phosphorylated

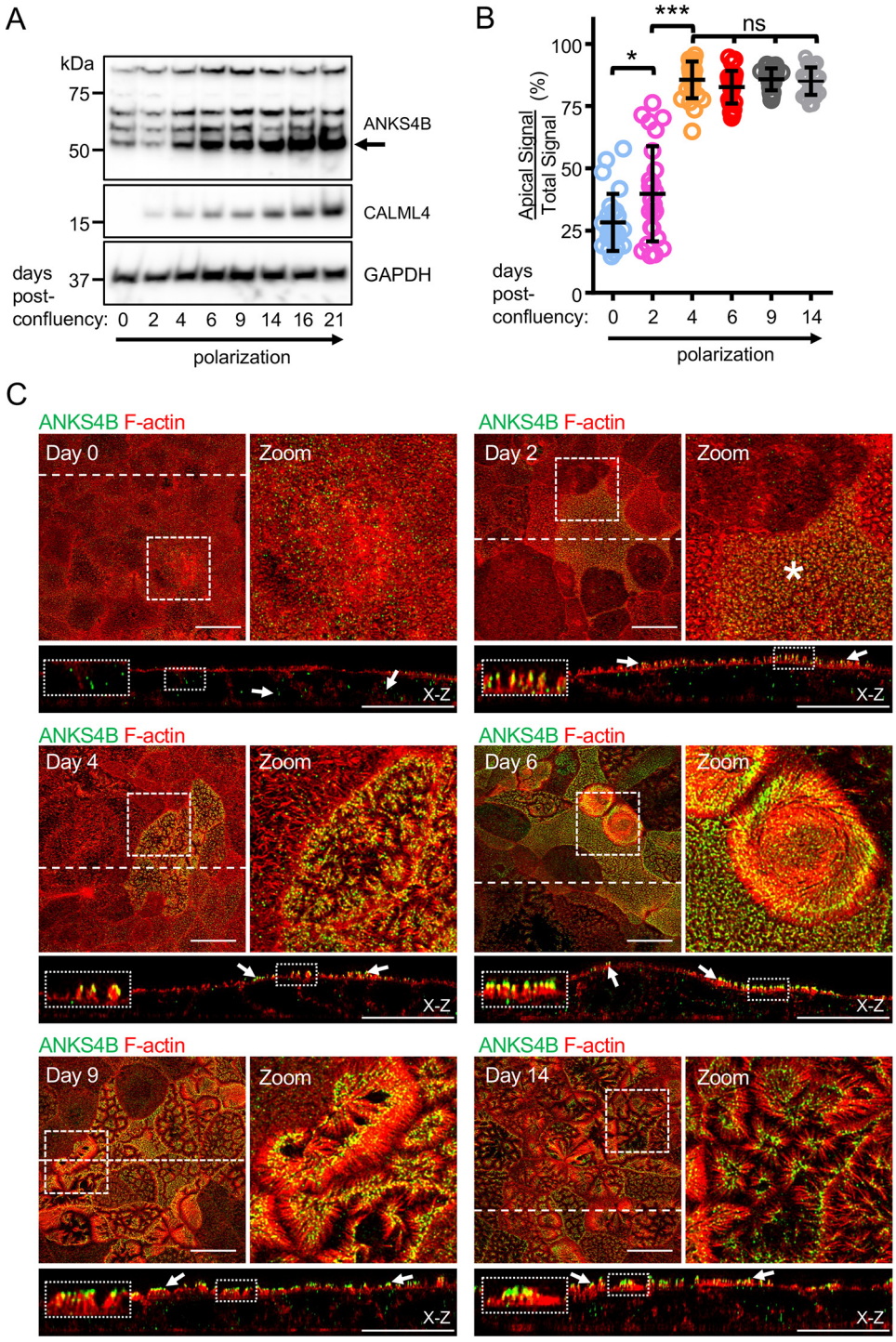

Figure 1. Expression and localization of ANKS4B across a polarization time course in CACO-2$_{BBE}$ cells. *A*, immunoblot analysis of a CACO-2$_{BBE}$ differentiation time series for expression of ANKS4B and CALML4. GAPDH served as a loading control. ANKS4B is detected across the entire time series as multiple bands, with the lowest-mass species (denote by an *arrow*) exhibiting a marked increase in total cellular levels during polarization. *B*, scatter plot quantification of the apical:total signal ratio of endogenous ANKS4B across a differentiation time series in CACO-2$_{BBE}$ cells. ANKS4B becomes apically enriched at the onset of cell polarization and BB assembly. The data are derived from three independent immunostaining experiments. At least 25 apical:total signal ratio data points were collected from cells for each plot variable. *ns*, not significant. *, $p < 0.01$; ***, $p < 0.0001$, *t* test. *Bars* indicate means ± S.D. *C*, confocal images of CACO-2$_{BBE}$ cells stained for endogenous ANKS4B (*green*) and F-actin (*red*) across a differentiation time series. The *boxed regions* in *en face* views denote areas in the zoomed panels. The *dashed lines* indicate the positions where the *x–z* sections were taken. The *arrows* in the *x–z* sections point to examples of localization. The *boxed regions* in the *x–z* sections show zoomed examples of localization. The *asterisk* in the *day 2* zoomed panel denotes a cell with apical ANKS4B. *Scale bars*, 20 μm.

form of Ezrin–Radixin–Merlin (ERM) family members that function as cytoskeletal-membrane cross-linkers (26). Ezrin is the principal ERM protein expressed in the gut epithelia (27, 28), with the active phosphorylated form (pThr^{567}) found highly enriched in BB microvilli along the entire crypt–villus axis (29). We first used the phospho-ERM signal to assess the

relative length of microvilli, and hence their maturity, along the crypt–villus axis in our tissue sections (Fig. S1*C*, see *top panel* for examples of length demarcations). Microvilli found in the crypt domain and at the villus base were short and immature (Fig. S1, *B* and *D*). Microvillar length rapidly increased until the mid-villus position, where it reached a mature length of ~1.8 μm toward the distal position of the villus (Fig. S1*D*). Confocal imaging revealed ANKS4B expression in both mature enterocytes on the villus surface and differentiating cells that reside in the crypt (Fig. S1*B*). However, the immature microvilli within the crypt were largely devoid of apical ANKS4B signal. Calculation of the ratio of apical to cytosolic signal of ANKS4B in enterocytes along the crypt–villus axis demonstrated that ANKS4B becomes apically enriched just prior to the enterocytes emerging from the crypt domain onto the villus surface (Fig. S1*E*; see also Fig. S1*C*, *bottom panels* for examples of cell compartment demarcations). Even at this early stage, ANKS4B signal could be seen at the distal tips of these still immature BB microvilli. Similar to microvillar length, apical signal of ANKS4B increased until the mid-villus position, where it reached its stable level of ~10-fold enrichment over the cytosol (Fig. S1*E*). Together, these results suggest that ANKS4B targets to the apical domain of enterocytes after the initial genesis of BB microvilli, consistent with its proposed role in organizing microvilli during BB assembly.

ANKS4B utilizes a cryptic targeting sequence to localize to the BB

It was previously shown that an N-terminal fragment (aa 1–252) of ANKS4B, containing the conserved ankyrin repeat domain, exhibited robust targeting to the BB when expressed as an EGFP-fusion protein in CACO-2_{BBE} cells (9). To begin to characterize the underlying mechanism governing apical targeting of ANKS4B, we performed a more refined structure–function analysis of this region of the scaffold. We divided the N-terminal fragment into two separate constructs: the predicted minimal ankyrin repeat domain (referred to as ANKR-$_{min}$; aa 1–126) and a construct containing the unannotated sequence connecting the $ANKR_{min}$ to the CEN domain, which we refer to as the Linker segment (LK; aa 119–252) (Fig. 2*A*). A cursory analysis of this LK segment using the PROSITE database revealed no similarity to any recognizable structured domain (30). We stably expressed these constructs as EGFP-fusion proteins in CACO-2_{BBE} cells, along with full-length and the N-terminal fragment (denoted here as ANKR–LK) of ANKS4B for reference. The cells were cultured for 12 days to allow them to form a well-structured BB before imaging. As previously seen, the ANKR–LK fragment of ANKS4B displayed an enhanced ability to target to apical microvilli compared with full-length ANKS4B (Fig. 2, *B, C,* and *G*; see Fig. S2, *A–C*, for representative examples of cells displaying high efficiency targeting, low efficiency targeting, and no targeting). In contrast, the isolated $ANKR_{min}$ domain exhibited low level apical targeting and did not recapitulate levels seen with the entire ANKR–LK construct (Fig. 2, *D* and *G*). This suggests that the $ANKR_{min}$ domain likely only plays an ancillary role in localizing ANKS4B to apical microvilli. Surprisingly, the isolated LK segment exhibited striking targeting to the BB that fully recapitulated the levels seen with the entire ANKR–LK fragment (Fig. 2, *E* and *G*). Importantly, we observed no significant apical targeting of EGFP alone when expressed in CACO-2_{BBE} cells (Fig. 2, *F* and *G*).

We next sought to determine whether apical targeting of the LK segment correlated with the appearance of clustering microvilli on the surface of CACO-2_{BBE} cells, which would be indicative of active IMAC in these protrusions. For this analysis, we binned EGFP–LK–positive cells according to their expression levels of the fusion protein (either low or high) and whether they exhibited either clustering or nonclustering microvilli (see Fig. S3, *A* and *B*, for representative examples). As a control, we used CACO-2_{BBE} cells expressing CDHR2–EGFP, which potently induces microvillar clustering (Fig. S3*C*) (8). Although CDHR2–EGFP expression was strongly associated with the appearance of microvillar clustering, we observed that high levels of apical EGFP–LK could often be seen in cells that had disorganized nonclustering microvilli (Fig. 3*A* and Fig. S3*A*). This suggests that the isolated LK segment on its own does not recruit active IMAC to protrusions to induce microvillar clustering. This led us to question whether a variant of ANKS4B lacking the LK segment could still support IMAC-mediated microvillar clustering. It has previously been shown that the loss of ANKS4B in CACO-2_{BBE} cells abolishes microvillar clustering (9), demonstrating that ANKS4B is strictly required for IMAC function (Fig. S3, *D* and *E*). To test the importance of the LK segment in ANKS4B function during BB assembly, we stably expressed EGFP-tagged KD refractory versions of full-length and ANKS4B ΔLK in our ANKS4B KD CACO-2_{BBE} cells. Although full-length ANKS4B was able to successfully rescue microvillar clustering, the variant lacking the LK segment failed to both target to the apical domain and rescue microvillar clustering (Fig. 3, *B* and *C*). In sum, these results identify a previously unappreciated apical targeting sequence in ANKS4B that is required for the function of the scaffold in IMAC-mediated BB assembly.

ANKS4B LK segment targeting does not perturb endogenous IMAC components

Endogenous ANKS4B targets to the distal tips of BB microvilli where it is a component of the cytoplasmic complex associated with CDHR2 (9). ANKS4B forms a stable tripartite complex with Myo7b and USH1C, with USH1C further associating with the cytoplasmic tail of CDHR2 to promote correct distal tip targeting of this protocadherin (Fig. S4*A*) (9). We questioned whether the LK segment of ANKS4B exhibited similar distal tip-targeting properties compared with endogenous IMAC components. To assess this, we performed line-scan analysis to determine the distribution of EGFP–LK along the axis of microvilli from CACO-2_{BBE} cells stably transduced with this construct. We used EPS8L3 (epidermal growth factor receptor kinase substrate 8-like protein 3) as a control, which served as an example of a non-IMAC protein that targets to the distal tips of microvilli. EPS8L3 is highly expressed in the enterocyte BB (31), where it functions to cap the plus-ends of F-actin filaments (32). Although overexpressed EGFP-EPS8L3 targeted

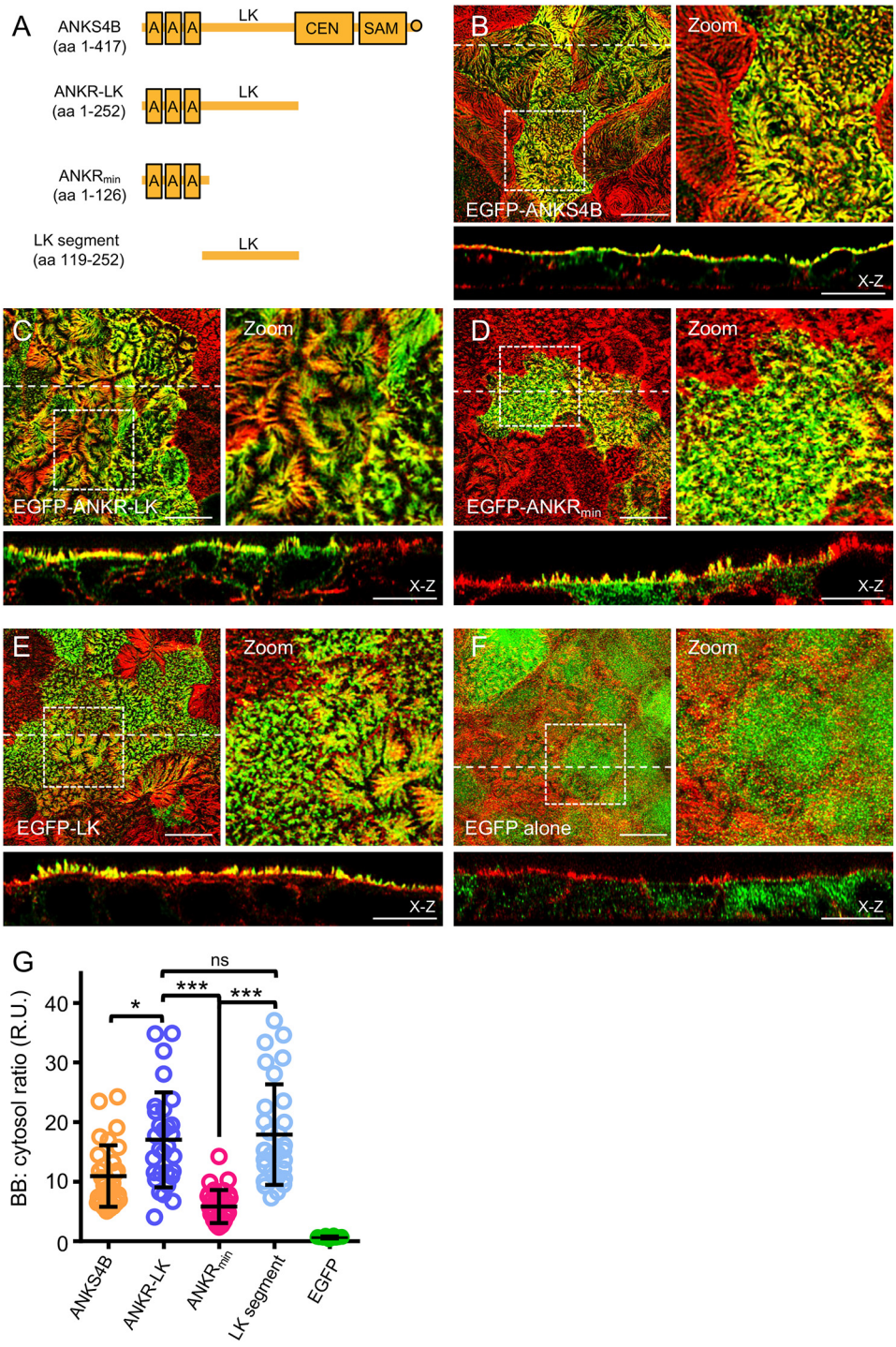

Figure 2. Identification of an apical targeting sequence in ANKS4B. *A*, constructs used to map the apical targeting sequence of ANKS4B. *B–F*, confocal images of 12-day polarized CACO-2_{BBE} cells stably expressing various EGFP-tagged ANKS4B constructs. The ANKS4B LK segment exhibits robust apical targeting. The *boxed regions* denote areas in the zoomed panels for each image set. The *dashed lines* indicate the positions where the *x–z* sections were taken; the *x–z* sections are shown below each *en face* image. *Scale bars*, 10 μm. *G*, scatter plot quantification of the BB:cytosol ratios of EGFP signal for all EGFP-fusion constructs tested. The data are derived from three independent immunostaining experiments; at least 30 BB:cytosol ratio data points were collected from cells for each plot variable. *ns*, not significant. *, $p < 0.01$; ***, $p < 0.0001$, *t* test. The *bars* indicate means ± S.D.

exclusively to the distal tips of BB microvilli, line-scan analysis of EGFP–LK revealed that it was found along the entire microvillar axis (Fig. S4*B*), mirroring the distribution of F-actin in microvilli.

We further explored whether overexpression of EGFP–LK could perturb the normal targeting of CDHR2 and its associated cytoplasmic complex, perhaps functioning as a dominant negative against correct tip targeting of the IMAC. We stained our stable EGFP–LK CACO-2_{BBE} cell line for endogenous CDHR2, USH1C, CALML4, and Myo7b and performed line-scan analysis to determine the relative localization of the EGFP signal compared with the endogenous IMAC components.

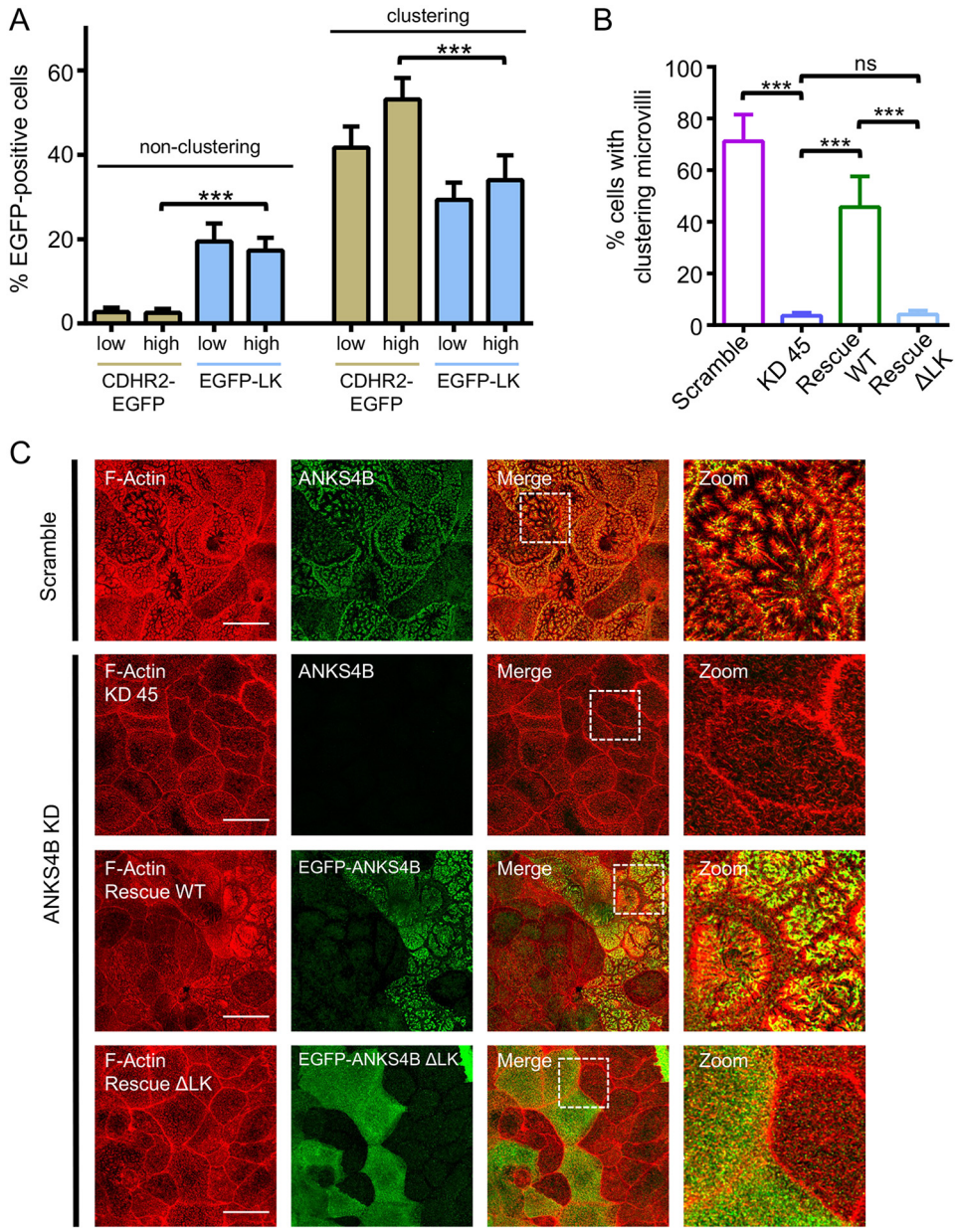

Figure 3. ANKS4B LK segment does not induce microvillar clustering but is required for ANKS4B function in BB assembly. *A*, quantification of microvillar clustering as a function of EGFP–LK ($n = 356$ cells) or CDHR2–EGFP expression levels ($n = 367$ cells) in 12-day polarized CACO-2_{BBE} monolayers. Although CDHR2–EGFP expression potently induced microvillar clustering, the EGFP–LK expression did not promote microvillar clustering. ***, $p < 0.0001$, *t* test. The *bars* indicate means ± S.D. *B*, quantification of microvillar clustering in nontransduced, scramble, ANKS4B KD, and ANKS4B rescue CACO-2_{BBE} cell lines. The cells were allowed to polarize for 12 days. The ANKS4B LK segment is essential for the ability of the scaffold to support IMAC-mediated microvillar clustering and BB assembly. For quantification of rescue cell lines, only EGFP-positive cells were scored: scramble control, $n = 384$ cells; ANKS4B KD, $n = 345$ cells; ANKS4B KD rescue EGFP–ANKS4B, $n = 256$ cells, ANKS4B KD rescue EGFP–ANKS4B ΔLK, $n = 287$ cells. *ns*, not significant. ***, $p < 0.0001$, *t* test. The *bars* indicate means ± S.D. *C*, confocal images of 12-day polarized CACO-2_{BBE} cells stably expressing either a scramble shRNA construct, an shRNA targeting ANKS4B (KD 45), or an shRNA targeting ANKS4B (KD 45) along with refractory variants of EGFP–ANKS4B WT or EGFP–ANKS4B ΔLK. The cells were stained for F-actin (*red*) and either ANKS4B (*green*) for scramble and KD cell lines or EGFP (*green*) for rescue lines. The refractory variant of ANKS4B lacking the LK segment fails to rescue microvillar clustering in ANKS4B KD cells. The *boxed regions* denote areas in the zoomed panels for each image set. *Scale bars*, 20 μm.

Confocal imaging of these samples revealed that the distal tip targeting of endogenous IMAC components were not impacted by the overexpression of EGFP–LK (Fig. 4, *A–D*). In agreement with this, protein pulldown analysis did not detect an interaction between the LK segment and CDHR2, CDHR5, USH1C, or Myo7b (Fig. S4, *C–E*). Interestingly, our pulldown analysis did reveal that the LK segment was able to interact with itself, although this interaction was masked in the full-length protein by the presence of the $ANKR_{min}$ domain (Fig. 5*A*). To assess whether apical targeting of the LK segment was due to an interaction with endogenous ANKS4B, we stained our stable EGFP–LK CACO-2_{BBE} cell line using a mAb that specifically recognizes the CEN domain of ANKS4B and does not cross-react with the LK segment (Fig. S5). Identical to the other CDHR2-associated factors, endogenous ANKS4B was not displaced from the distal tips of BB microvilli when EGFP–LK was

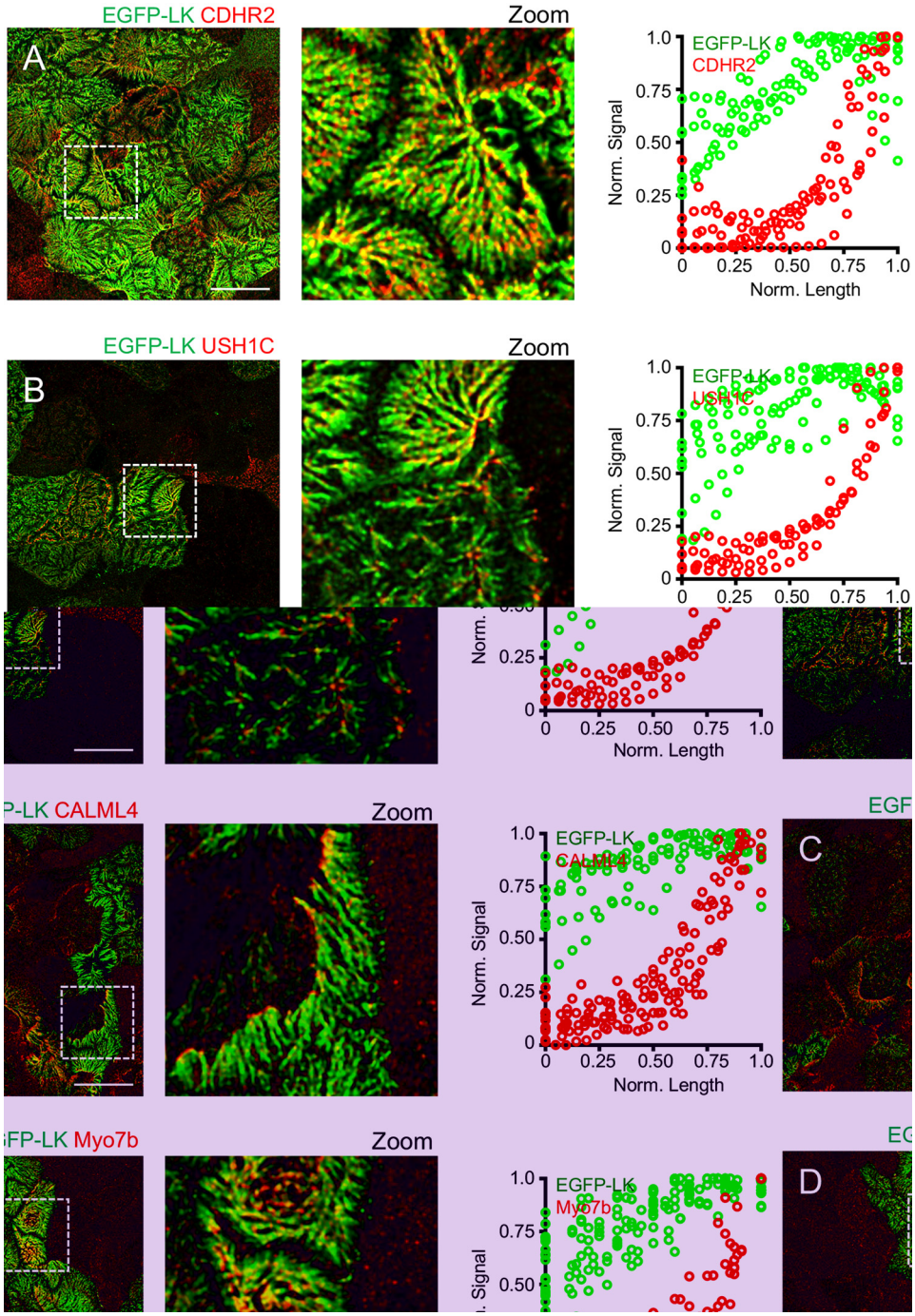

Figure 4. ANKS4B LK segment does not perturb distal tip targeting of endogenous IMAC components. *A–D, left panels*, confocal images of 12-day polarized CACO-2_{BBE} monolayers expressing EGFP–LK stained for EGFP (*green*) and endogenous IMAC components (*red*): CDHR2, USH1C, CALML4, and Myo7b. Components of the IMAC retain their localization at the distal tips of BB microvilli even when the LK segment of ANKS4B is overexpressed. The *boxed regions* denote areas in the zoomed panels. *Scale bars*, 20 μm. *Right panels*, line-scan analysis of EGFP (*green*) and endogenous IMAC component (*red*) signal intensity collected parallel to the microvillar axis in EGFP–LK CACO-2_{BBE} cells. Microvillar length has been normalized (*Norm.*), where 0 = base of microvilli, and 1 = distal tip of microvilli. Each plot shows a collection of at least six normalized scans for each signal channel.

overexpressed (Fig. 5*B*). We further confirmed that targeting of the isolated ANKS4B LK sequence was not dependent upon interaction with endogenous ANKS4B by expressing the EGFP–LK construct in our ANKS4B KD cell line. Consistent with our previous data, the EGFP–LK localized to the BB in the ANKS4B KD background (Fig. 5*C*). Altogether, these results suggest that the ANKS4B LK segment exhibits the ability to target to the BB independent of a direct interaction with the other known IMAC components.

Analysis of the ANKS4B LK segment reveals sequence motifs necessary for apical targeting

To begin to shed light on the structural determinants that promote apical targeting of the ANKS4B LK segment, we

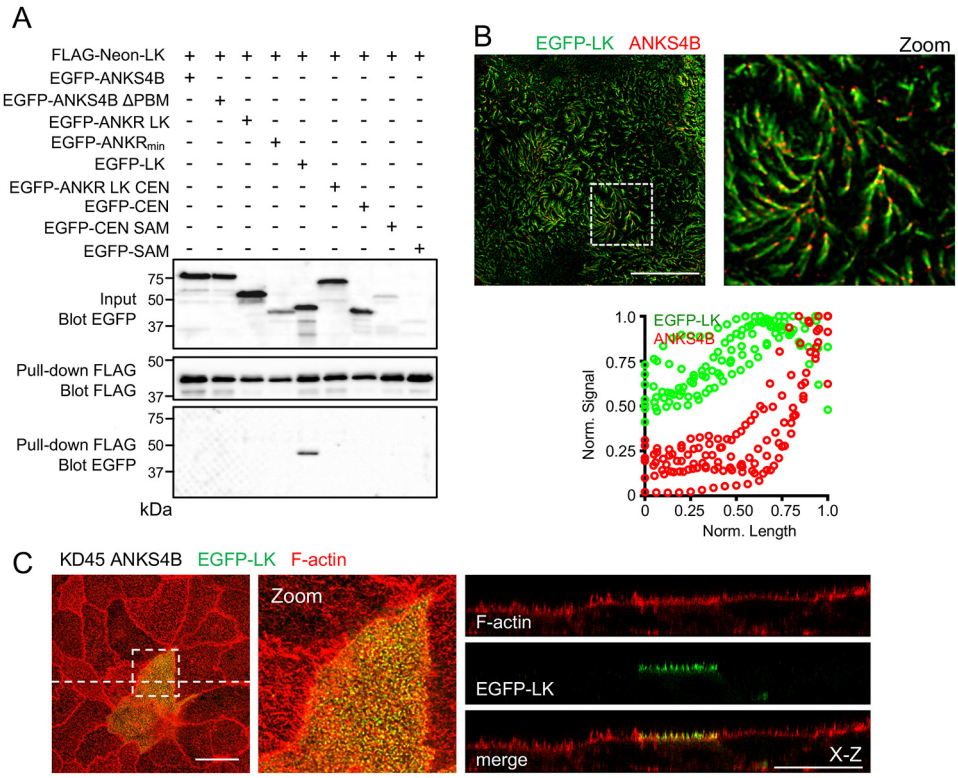

Figure 5. ANKS4B LK segment apical targeting does not depend on interaction with endogenous ANKS4B. *A*, testing for binding interactions between ANKS4B LK segment and the domains of ANKS4B. FLAG-tagged mNEON-LK served as bait, whereas EGFP-tagged ANKS4B fragments served as prey. The blots show that the LK segment of ANKS4B can interact with itself. *B*, *top panels*, confocal image of 12-day polarized CACO-2$_{BBE}$ monolayers expressing EGFP–LK stained for EGFP (*green*) and endogenous ANKS4B (*red*). Endogenous ANKS4B retains its localization at the distal tips of BB microvilli even when the LK segment of ANKS4B is overexpressed. The *boxed region* denotes the area in the zoomed panel. *Scale bar*, 20 μm. *Bottom panel*, line-scan analysis of EGFP (*green*) and endogenous ANKS4B (*red*) signal intensity collected parallel to the microvillar axis in EGFP–LK CACO-2$_{BBE}$ cells. Microvillar length has been normalized (*Norm.*), where 0 = base of microvilli, and 1 = distal tip of microvilli. Each plot shows a collection of at least six normalized scans for each signal channel. *C*, confocal image of 12-day polarized CACO-2$_{BBE}$ cells stably expressing an shRNA targeting ANKS4B (KD 45) along with EGFP–LK. The cells were stained for F-actin (*red*) and EGFP (*green*). The EGFP–LK construct still retains the ability to target to the BB in the absence of endogenous ANKS4B. The *boxed region* denotes the area in the zoomed panel. The *dashed line* indicates the position where the *x–z* section was taken; The different channels along with a merge image of the *x–z* section are shown to the *right*. *Scale bars*, 20 μm.

performed a detailed sequence motif analysis of this region of the scaffold. We detected a potential coiled-coil (CC) at the beginning of the LK segment (Fig. 6, *A* and *D*) followed by a sequence rich in serine residues, which we dubbed the serine-rich patch (SRP; Fig. 6, *B* and *D*). Finally, a basic-hydrophobic (BH) score algorithm (33) detected a putative basic-hydrophobic-basic (BHB) membrane-binding repeat sequence motif directly after the SRP (Fig. 6, *C* and *D*). When expressed as EGFP-fusion proteins in CACO-2$_{BBE}$ cells, however, no one sequence motif from the ANKS4B LK segment was able to target efficiently to the BB (Fig. 6, *A–C* and *E*). Both the SRP and BHB were found largely in the cytosol, whereas the CC motif accumulated in the nucleus. Furthermore, CC–SRP or SRP–BHB concatenations also did not recapitulate the level of targeting seen with the full LK segment, although the SRP–BHB fragment did display a slight enrichment in microvilli (Fig. S6, *A–E*).

We probed the importance of these motifs for ANKS4B apical targeting using a series of internal deletion mutants lacking these individual sequences (Fig. S6*F*). The apical targeting ability of these internal deletion constructs were assessed compared with both full-length and ANKS4B ΔLK constructs (Fig. S6*F*). Deletion of the CC and BHB motifs resulted in diminished targeting of ANKS4B, whereas deletion of the SRP had less of an effect (Fig. S6, *G–L*). Interestingly, internal deletion of the SRP often resulted in the protein becoming restricted to the distal tips of BB microvilli. Taken together, these results demonstrate that the CC and BHB motifs are necessary for the targeting activity of the ANKS4B LK segment, whereas the SRP could possibly play a role in regulating incorporation of ANKS4B specifically at the distal tips of BB microvilli.

The USH1G LK segment lacks the ability to target to the BB

The functional homolog of ANKS4B that operates in sensory epithelia as part of the Usher complex is the scaffold USH1G. ANKS4B and USH1G have an identical domain structure and exhibit an overall sequence identity of 48% (Fig. S7*A*). The highest identity is found between the ANKR$_{min}$ domains of the two scaffolds (~70%), whereas the LK segments have the lowest identity at ~24%. Homologous to ANKS4B, USH1G uses its CEN domain to bind to Myo7a with moderate affinity, whereas its SAM–PBM domain interacts with USH1C with low-nanomolar affinity (12, 13). Given the appreciable homology between ANKS4B and USH1G, we performed a structure–function analysis of the different domains of USH1G to assess whether the BB-targeting ability has been conserved

between these two scaffolds (Fig. 7*A*). When expressed as an EGFP fusion in CACO-2_{BBE} cells, full-length USH1G exhibited a low-level ability to target to the BB (Fig. 7, *B* and *H*). Analysis of the individual domains suggests that this targeting is primarily mediated by the conserved $ANKR_{min}$ domain (Fig. 7, *C–F* and *H*). In stark contrast to ANKS4B, the LK segment of USH1G failed to target to the BB and was found enriched in the nucleus (Fig. 7, *D* and *H*). Sequence analysis of the USH1G LK segment revealed a weakly predicted CC motif and a region corresponding to the SRP found in ANKS4B (Fig. S7, *B* and *C*). A potential BHB motif was also detected in the same position as the ANKS4B BHB motif; however, its BH score is significantly lower compared with ANKS4B (Fig. S7*D*). To confirm that divergence in the LK segment of USH1G underlies its inability to efficiently target to the enterocyte apical domain, we created a chimera in which we swapped the LK segment of ANKS4B into USH1G (Fig. 7*A*). As expected, this chimera exhibited enhanced targeting to apical microvilli (Fig. 7, *G* and *H*).

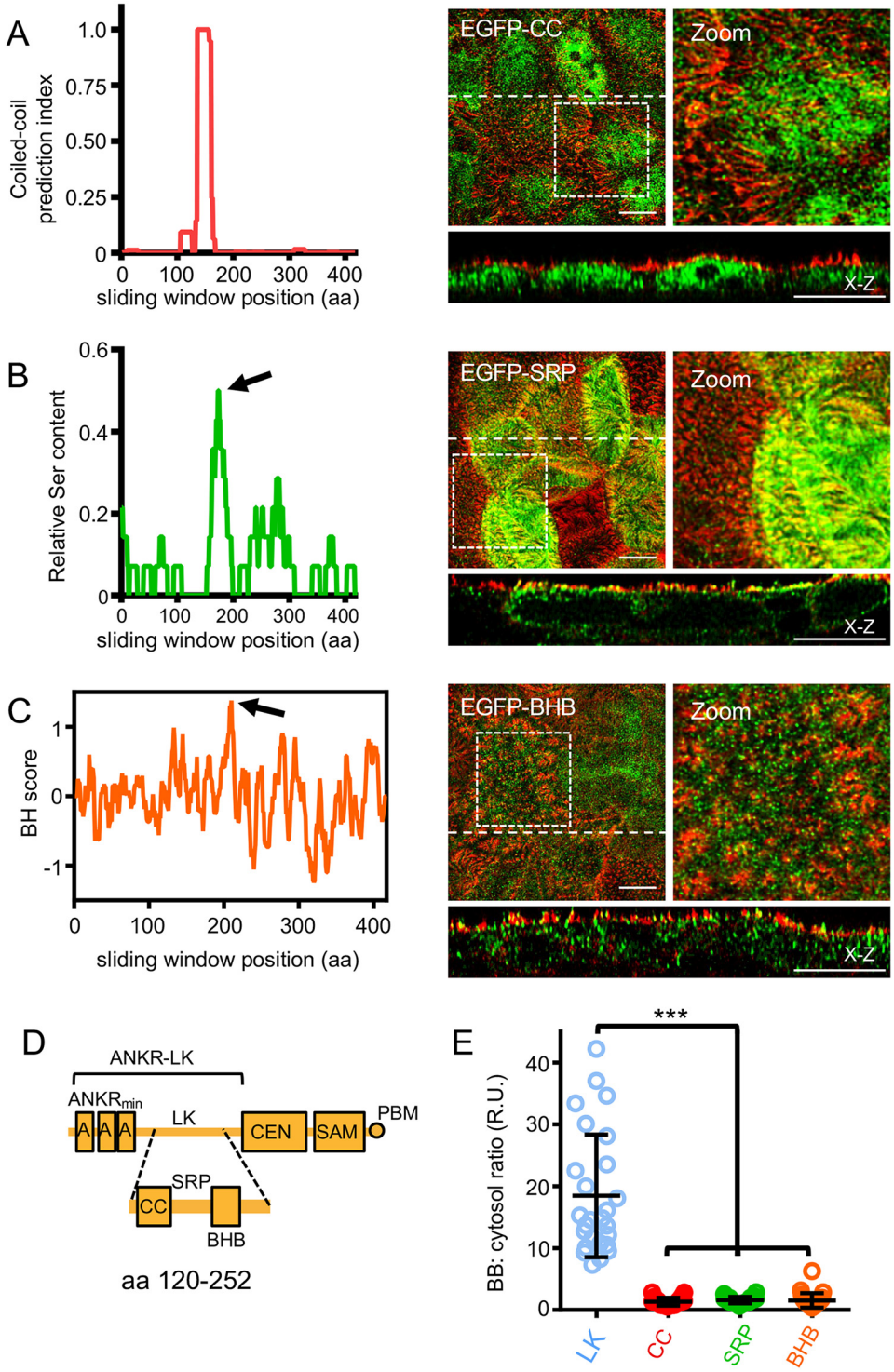

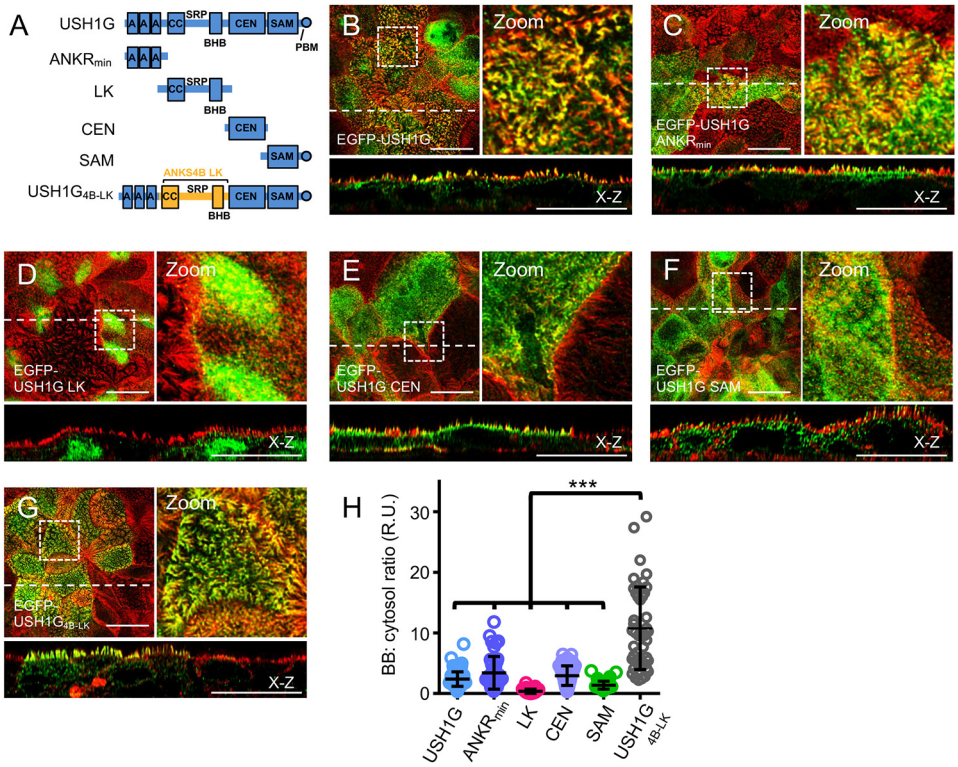

Figure 7. Structure–function analysis of the Usher complex scaffold USH1G in CACO-2$_{BBE}$ cells. *A*, constructs used to assess the BB-targeting ability of the Usher complex scaffold, USH1G. *B–G*, confocal images of 12-day polarized CACO-2$_{BBE}$ cells stably expressing EGFP-fusion constructs tested. USH1G exhibits low-level targeting to the apical domain when expressed in CACO-2$_{BBE}$ cells because of a divergence in its LK sequence compared with ANKS4B. The *boxed regions* denote areas in the zoomed panels for each figure. The *dashed lines* indicate the positions where the *x–z* sections were taken. The *x–z* sections are shown below each *en face* image. *Scale bars*, 10 μm. *H*, scatter plot quantification of the BB:cytosol ratios of EGFP signal for all EGFP-fusion constructs tested. The data are derived from three independent immunostaining experiments. At least 50 BB:cytosol ratio data points were collected from cells for each plot variable. ***, $p < 0.0001$, *t* test. The *bars* indicate means ± S.D.

We further used a chimeric approach to explore how differences in the CC and BHB motifs between ANKS4B and USH1G impact apical targeting (Fig. 8*A*). When the ANKS4B CC motif was fused to an USH1G SRP–BHB fragment, this chimera exhibited a moderate increase in apical targeting compared with USH1G LK (Fig. 8, *B* and *F*). In contrast, a significantly higher level of apical targeting was observed when the USH1G CC motif was fused to an SRP–BHB fragment of ANKS4B (Fig. 8, *C* and *F*). Given that we saw that the ANKS4B SRP sequence has a more dispensable role in apical targeting (Fig. S6*K*), these results suggest that differences in the BHB motif between ANKS4B and USH1G may represent a point of specialization of ANKS4B that allows it to target to BB microvilli in the gut. To directly test the importance of the ANKS4B BHB motif, we performed a sequence alignment of the LK segment of ANKS4B orthologs across a diverse set of species to identify highly conserved residues within the BHB motif that might be important for its apical targeting properties (Fig. S8*A*). This analysis revealed a core set of basic and hydrophobic residues found in this motif that are widely conserved. Strikingly, mutation of a single conserved basic residue within this cluster was enough to perturb apical targeting of the ANKS4B LK segment (Fig. 8, *D*, *E*, and *G*). Mutating both hydrophobic and basic positions in the BHB motif of ANKS4B lowered the BH score to the same level as USH1G (Fig. S8*B*) and completely abolished apical targeting of the ANKS4B LK segment (Fig. S8,

Figure 6. Sequence analysis of the ANKS4B LK segment identifies structural motifs. *A*, *left panel*, analysis of ANKS4B with the CC prediction program COILS, which identifies a potential coiled-coil motif at the beginning of the LK segment. *Right panel*, confocal image of a 12-day polarized CACO-2$_{BBE}$ monolayer expressing EGFP–ANKS4B CC stained for EGFP (*green*) and F-actin (*red*). The isolated CC motif fails to target to the apical domain when expressed in CACO-2$_{BBE}$ cells. The *boxed region* denotes the area in the zoomed panel. The *dashed line* indicates the position where the *x–z* section was taken; the *x–z* section is shown below the *en face* image. *Scale bar*, 15 μm. *B*, *left panel*, analysis of the relative Ser content of ANKS4B, which identifies a region rich in Ser residues (*arrow*) that follows the CC motif. *Right panel*, confocal image of a 12-day polarized CACO-2$_{BBE}$ monolayer expressing EGFP–ANKS4B SRP stained for EGFP (*green*) and F-actin (*red*). The isolated SRP motif fails to target to the apical domain when expressed in CACO-2$_{BBE}$ cells. The *boxed region* denotes the area in the zoomed panel. The *dashed line* indicates the position where the *x–z* section was taken; the *x–z* section is shown below the *en face* image. *Scale bar*, 15 μm. *C*, *left panel*, analysis of ANKS4B using a BH score algorithm identifies a potential BHB motif (*arrow*) following the SRP sequence. *Right panel*, confocal image of 12-day polarized CACO-2$_{BBE}$ monolayer expressing EGFP–ANKS4B BHB stained for EGFP (*green*) and F-actin (*red*). The isolated BHB motif fails to target to the apical domain when expressed in CACO-2$_{BBE}$ cells. The *boxed region* denotes the area in the zoomed panel. The *dashed line* indicates the position where the *x–z* section was taken; the *x–z* section is shown below the *en face* image. *Scale bar*, 15 μm. *D*, cartoon showing the revised domain structure of ANKS4B. *E*, scatter plot quantification of the BB:cytosol ratios of EGFP signal for all EGFP-fusion constructs tested. No motif found in the LK segment of ANKS4B exhibits apical targeting on its own when expressed in CACO-2$_{BBE}$ cells. The data are derived from three independent immunostaining experiments. At least 25 BB:cytosol ratio data points were collected from cells for each plot variable. ***, $p < 0.0001$, *t* test. The *bars* indicate means ± S.D.

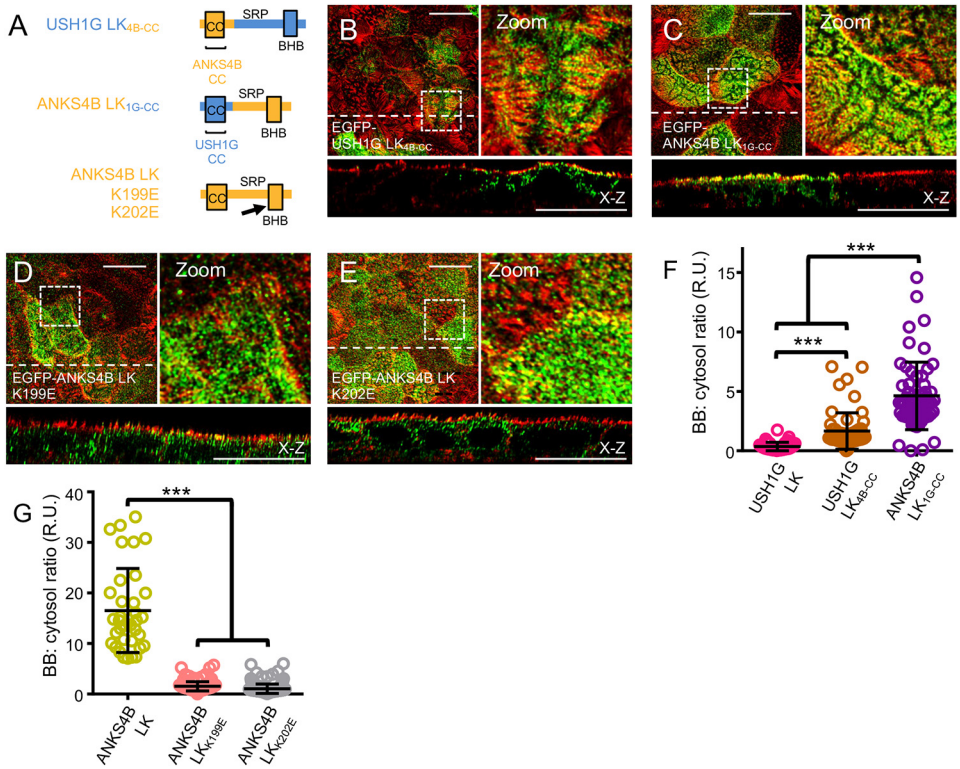

Figure 8. The BHB motif of ANKS4B is essential for ANKS4B LK segment targeting. *A*, diagram of the constructs used to interrogate the apical targeting contribution of motifs found in the ANKS4B LK segment through chimeric and point mutation (*arrow*) analysis. *B–E*, confocal images of 12-day polarized CACO-2_{BBE} cells stably expressing EGFP-fusion constructs tested. The BHB motif plays an essential role in apical targeting. The *boxed regions* denote areas in the zoomed panels for each figure. The *dashed lines* indicate the positions where the *x–z* sections were taken; the *x–z* sections are shown below each *en face* image. *Scale bars*, 10 μm. *F* and *G*, scatter plot quantification of the BB:cytosol ratios of EGFP signal for all EGFP-fusion constructs tested. The data are derived from three independent immunostaining experiments. At least 50 BB:cytosol ratio data points were collected from cells for each plot variable. ***, $p < 0.0001$, *t* test. The *bars* indicate means ± S.D.

C and *D*). In sum, these results identify a functional divergence between ANKS4B and USH1G and further highlight the importance of the putative membrane-binding BHB motif in the apical targeting mechanism of ANKS4B.

Recombinant ANKS4B LK segment forms a functional oligomer

To begin to investigate the biophysical properties of the LK segment of ANKS4B, we attempted to express and purify recombinant ANKS4B LK from bacteria to test its oligomerization properties. Although the isolated LK segment on its own expressed poorly in bacteria, we discovered that fusing this fragment of ANKS4B to a mNEON tag allowed for soluble fusion protein to be recovered in quantities amenable to analysis (Fig. 9*A* and Fig. S9*A*). We explored the oligomeric state of mNEON–ANKS4B LK using size-exclusion chromatography. As controls, we used mNEON alone, which is monomeric (34), and mNEON fused to the CC motif of Myosin-10 (Myo10 CC), which forms an antiparallel dimer in solution (35). Both controls expressed well and were purified to near homogeneity (Fig. 9*A* and Fig. S9*B*). An added advantage of using Myo10 CC as a control is that it is similar in molecular weight compared with the LK segment of ANKS4B (Fig. 9*A*), which allowed us to make a direct comparison between their behavior. We observed that mNEON–ANKS4B LK eluted with a similar value from the size-exclusion column compared with mNEON–Myo10 CC, suggesting that the LK segment was also an oligomer (Fig. 9, *B* and *C*). Together, these data are consistent with our pulldown results (Fig. 5*A*) showing that the ANKS4B LK segment can form an oligomer.

To assess whether this recombinant ANKS4B LK segment protein was biologically active, we incubated the purified mNEON–ANKS4B LK protein with BBs isolated from polarized CACO-2_{BBE} cells (11). BBs were subsequently recovered after protein incubation using low-speed centrifugation, washed numerous times to remove unbound protein, and visualized for NEON signal using a blue light transilluminator. As a control, we used mNEON alone, which does not target to the apical domain when expressed in CACO-2_{BBE} cells. In contrast to our mNEON alone control, we observed robust mNEON–ANKS4B LK signal associated with the final BB pellet (Fig. 9*D*). We noted, however, that the mNEON–ANKS4B LK signal was relatively unstable (especially at room temperature), possibly being lost because of degradation. We observed similar behavior during our initial attempts to assess the oligomeric state of the protein when we ran our size-exclusion column at room temperature (Fig. S9*C*). Under these conditions, the recombinant mNEON–ANKS4B LK protein eluted primarily as degradation products (Fig. S9*D*). In sum, these data suggest that the recombinant oligomeric ANKS4B LK protein can functionally associate with BBs.

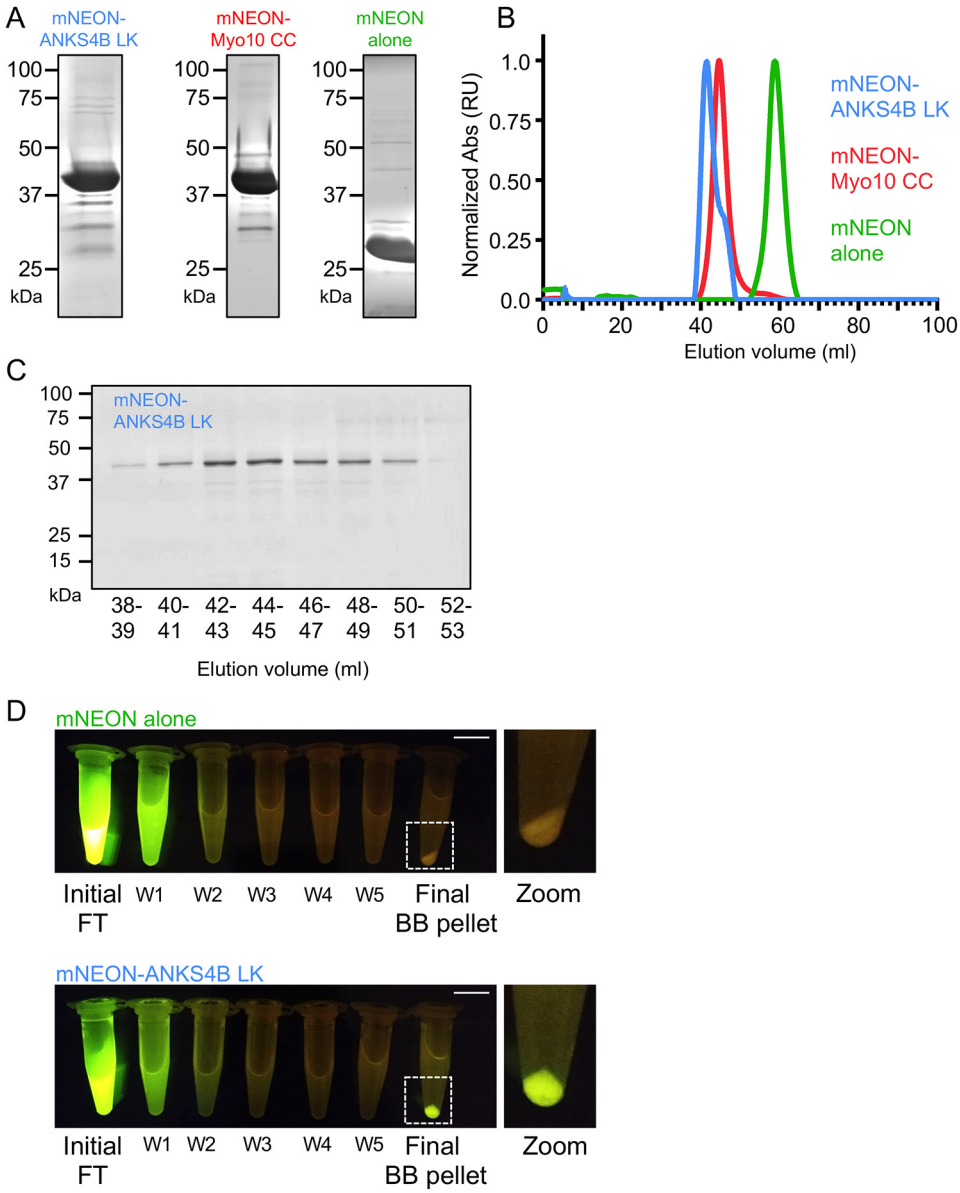

Figure 9. The LK segment of ANKS4B forms an oligomer. *A*, Coomassie Blue–stained SDS-PAGE analysis of mNEON–ANKS4B LK, mNEON–Myo10 CC, and mNEON alone. *B*, elution profile of the size-exclusion chromatography of purified recombinant mNEON–ANKS4B LK, mNEON–Myo10 CC, and mNEON alone. mNEON–ANKS4B LK elutes with a similar value compared with mNEON–Myo10 CC, which forms an antiparallel dimer in solution. *RU*, relative units. *C*, Coomassie Blue–stained SDS-PAGE analysis of the eluate peak from mNEON–ANKS4B LK size-exclusion chromatography. *D*, incubation of mNEON alone (*top panels*) or mNEON–ANKS4B LK protein (*bottom panels*) with BBs that were isolated from 21-day polarized CACO-2_{BBE} cells. NEON signal is visualized used a blue light transilluminator. For both mNEON alone and mNEON–ANKS4B LK, BBs were incubated with 100 μg of purified recombinant protein for 20 min. BBs were then recovered and washed five times to remove unbound protein. The flow-through (*FT*) supernatant of the initial incubation mixture, and supernatant from each wash (*W1–W5*) is shown for each series. The final tube for each series shows the BB pellet. mNEON–ANKS4B LK associates with the BB pellet, in contrast to mNEON alone. The *boxed regions* denote areas in the zoomed panels for each series. *Scale bars*, 1 cm.

Discussion

Currently, little is known about how the IMAC targets to and assembles in the apical domain of enterocytes during their polarization program. We previously observed that formation of a tripartite complex between ANKS4B, USH1C, and Myo7b occurs in an ordered manner, in which USH1C first activates both ANKS4B and Myo7b to allow for stable tripartite binding interactions (9). In agreement with this, ANKS4B and Myo7b both fail to target to apical microvilli in USH1C KO mice, resulting in severe BB assembly defects in this mouse model (8, 9). This may explain why patients with genetic defects in USH1C have been reported to suffer from severe inflammatory enteropathy with intractable diarrhea (20). In the absence of functional USH1C, the IMAC is unable to promote correct assembly of the intestinal BB, which could lead to perturbed barrier function in the gut. We undertook the present study to further explore the molecular determinants that mediate apical assembly of the IMAC, focusing on the contribution of the scaffold ANKS4B.

The role of BHB motifs in cellular localization

We used structure–function analysis to define a region of the scaffold ANKS4B that specifically targets to BB microvilli. Our

results demonstrate that this targeting domain, which we dubbed the ANKS4B LK segment, localizes to apical microvilli independent of a direct interaction with the other known IMAC components, suggesting that it could function to "seed" the IMAC in the apical domain during the initial stages of BB assembly. Sequence analysis of the ANKS4B LK segment revealed the presence of a strongly predicted BHB motif that, when mutated, abolished BB targeting. BHB motifs are detected as two basic sequences separated by a hydrophobic sequence, although they lack a canonical consensus sequence and do not exhibit appreciable sequence homology between occurrences (33, 36). In agreement with this, BHB motifs are thought to associate with acidic phospholipids as unstructured membrane-binding sites. BHB motifs have been shown to be critical for the cellular localization and function of members of the class 1 myosins, which often play a role in linking the actin cytoskeleton to cellular membranes. These include members of the class 1 myosins from *Dictyostelium* (37), as well as mammalian Myo1a (Myosin-1a) (38). Pertinent to our study, mammalian Myo1a is highly enriched in the enterocyte BB, where it plays a critical role in linking the microvillar membrane to the underlying F-actin core to promote BB structure. Loss of Myo1a results in BB defects in which the apical membrane appears to herniate away from the underlying cytoskeleton of enterocytes (39). Similar to our observations with ANKS4B, mutating the BHB motifs found in the tail domain of Myo1a perturbs proper BB localization of the myosin (38).

Although disrupting the BHB motif of ANKS4B abolished apical targeting, the isolated BHB sequence on its own did not display significant enrichment in the BB. This suggests that further sequences beyond the BHB motif of ANKS4B are necessary for apical targeting. We show that a putative CC sequence found upstream of the BHB motif in the ANKS4B LK segment also plays an essential role in mediating BB localization. Our preliminary characterization of the ANKS4B LK segment suggests that it can oligomerize, which may indicate that two or more of these sequences may need to self-associate before reaching a threshold level of membrane-binding activity that can mediate robust apical targeting in enterocytes. Going forward, it will be important to investigate the underlying determinants that allow the BHB motif of ANKS4B to function in apical targeting.

Functional comparison of ANKS4B and USH1G

Despite serving tissues with different physiological functions, the IMAC and Usher complex exhibit striking homology in both their composition and interactome. Indeed, each component of the core Usher complex has a functional homolog that operates in the IMAC (1). We speculated, however, that the individual components of each complex might be fine-tuned to function in their respective tissues of origin. With this in mind, we used a compare-and-contrast approach to shed light on the functional similarities and differences between ANKS4B in the IMAC and USH1G in the Usher complex. Both scaffolds are known to interact with USH1C and the myosin motor protein found in their complex (9, 12, 13). However, whether they share other similarities or differences in their properties was not previously known. USH1G has been shown to interact with other binding partners, including myomegalin, membrane-associated guanylate kinase inverted-2, and components of the intraflagellar transport system. This suggests that USH1G could participate in a variety of cellular functions beyond the Usher complex (40–42). Sequence analysis of the USH1G LK segment did detect weakly predicted CC and BHB motifs in similar positions compared with ANKS4B, and the LK segment of USH1G is also thought to promote oligomerization of the scaffold as we observed for ANKS4B (43, 44). Despite this, the USH1G LK segment failed to localize to the BB when expressed in CACO-2_{BBE} cells. This points to a divergence in function between the two scaffolds, where ANKS4B has become specialized to act as an apical targeting factor to localize the other cytosolic components of the IMAC to the BB domain, allowing them to form a stable complex at the microvillar tips. In agreement with this, genetic disruption of ANKS4B in CACO-2_{BBE} cells results in markedly reduced cellular levels of the other known IMAC components.

It is interesting to note that a specific splice isoform of USH1C found expressed during inner-ear development (conventionally known as the Harmonin-b isoform) has the ability to bind to and bundle F-actin (45). This activity is not found in the USH1C splice isoform (Harmonin-a) used in the IMAC. Whether USH1C, rather than USH1G, has evolved to play a role in targeting the Usher complex in hair cells by associating with the F-actin core of stereocilia will be an interesting question to pursue.

Structure–function and KD studies of individual IMAC components using the malleable CACO-2_{BBE} cell line suggest that all components are required to achieve correct targeting and function of the adhesion complex at the distal tips of BB microvilli (8–10). Mounting evidence suggests that this interdependency is likely directly encoded in the structure of the IMAC components. Biochemical and cell-based studies investigating the two scaffolds, USH1C and ANKS4B, have revealed that each are regulated by autoinhibition (9, 46). USH1C has been shown to adopt a closed conformation that controls its interaction with binding partners. This is mediated by intramolecular binding of its C-terminal PBM to its N-terminal NPDZ1 supramodule domain (46). Relevant to our study here, the targeting ability of ANKS4B is strictly regulated in the context of the full-length molecule. Deletion of the C-terminal PBM of ANKS4B, which blocks binding to USH1C, abolishes apical targeting of the scaffold (9). This suggests that the LK segment is either masked or in an inactive form in the full-length autoinhibited conformation of the scaffold. Understanding the mechanism of how the apical targeting ability of the LK segment of ANKS4B is regulated during BB assembly is a clear future goal.

Experimental procedures

Molecular biology

The human cDNA constructs used in this study are as follows: ANKS4B, GI: 148664245; USH1C, GI: 225690577; Myo7b, GI: 122937511; CDHR2, GI: 285002213; and CDHR5, GI: 285002197. The mouse Myo10 cDNA construct used in this study was GI: 130507684. DNA encoding these components

ASBMB

were generated by PCR and TOPO cloned into the pCR8 entry vector (Invitrogen). The domain boundaries for the Myo7b constructs used are as follows: Myo7b full-length tail (aa 916–2116), Myo7b MF1SH3 (aa 916–1542), and Myo7b SH3MF2 (aa 1501–2116). The domain boundaries for the ANKS4B constructs used are as follows: ANKS4B $ANKR_{min}$ (aa 1–126), ANKS4B LK (aa 119–252), ANKS4B CC (aa 119–173), ANKS4B SRP (aa 164–197), ANKS4B BHB (aa 187–252), ANKS4B CEN (aa 253–346), ANKS4B SAM (aa 348–417), ANKS4B ANKR–LK (aa 1–252), ANKS4B ANKRCEN (aa 1–346), and ANKS4B CENSAM (aa 253–417). The domain boundaries for the USH1C constructs used are as follows: NPDZ1 (aa 1–193), PDZ2 (aa 194–295), PDZ2CC (aa 194–451), PDZ3 (aa 379–553), CCPDZ3 (aa 294–553), NPDZ12 (aa 1–302), and PDZ2CCPDZ3 (aa 194–553). The domain boundaries for the USH1G constructs used are as follows: USH1G $ANKR_{min}$ (aa 1–124), USH1G LK (aa 120–294), USH1G CEN (aa 295–389), and USH1G SAM (aa 385–461). The domain boundary for Myo10 construct is Myo10 CC (aa 877–942). The protocadherin constructs used in this study are as follows: cytoplasmic domain of CDHR5 (aa 697–845) and cytoplasmic domain of CDHR2 (aa 1178–1310). The pINDUCER20 lentiviral vector (47) was modified to include an EGFP tag upstream of the Gateway recombination cassette to create pINDUCER20–EGFP–C1. This vector was used for the generation of stable cell lines expressing most of the constructs used in the study. Vectors used for expression of FLAG and Myc-tagged proteins in this study have been previously described (8, 9). Constructs used for the bacterial expression of the cytoplasmic domains (CDs) of the protocadherins have been previously described (8). The construct used for the bacterial expression of proteins fused to mNEON that contains an N-terminal hexahistidine tag were generate by cloning into the pNCS–mNEONGreen vector (Allelebiotech). The shRNA clones targeting ANKS4B were expressed in the pLKO.1 vector and correspond to TRC clones TRCN0000122345 and TRCN0000139080. These shRNAs have been previously validated (9). A nontargeting scramble shRNA cloned into the pLKO.1 vector was used as a control (Addgene; plasmid 1864). For rescue experiments, the QuikChange site-directed mutagenesis kit (Agilent, catalog no. 200523) was used to introduce refractory silent mutations into the region of ANKS4B targeted by the shRNA construct. The primers used for mutagenesis were RF45 sense (TCCTCTACTGCAGATTATCTCCAAAGCTTCCAAGTTCCCATGGTAG) and RF45 antisense (CTACCATGGGAACTTGGAAGCTTTGGAGATAATCTGCAGTAGAGGA).

Cell culture, lentivirus production, and stable cell line generation

CACO-2_{BBE}, HEK293T, and HEK293FT cells were cultured at 37 °C and 5% CO_2 in a humidified incubator using Dulbecco's modified Eagle's medium with high glucose and 2 mM L-glutamine. Medium was supplemented with 20% FBS for CACO-2_{BBE} cells and 10% FBS for HEK293T and HEK293FT cells. Lentivirus particles were generated by cotransfecting HEK293FT cells (10-cm dish at 80% confluency) with 6 μg of lentiviral overexpression plasmid with 4 μg of psPAX2 packaging plasmid and 0.8 μg of pMD2.G envelope plasmid using polyethylenimine reagent (Polysciences). The cells were incubated with transfection medium for 12 h, after which they were exchanged with fresh medium. The cells were subsequently incubated for 2 days to allow for lentiviral production into the medium. Medium containing lentiviral particles was collected and filtered with a 0.45-μm syringe filter. Lentiviral particles were concentrated and recovered using with Lenti-X concentrator reagent according to the recommended protocol (Clontech). For lentivirus transduction, CACO-2_{BBE} cells were grown to 90% confluency in T25 flasks. For lentiviral infection, the medium was first supplemented with 8 μg/ml Polybrene, after which ~300 μl of concentrated lentiviral particle solution was added. After 12 h of incubation with lentivirus, the cells were reseeded into 10-cm dishes and grown for 3 days. The cells were then reseeded into T182 flasks with medium containing 50 μg/ml of puromycin or 1 mg/ml G418 and passaged to select for stable integration.

Protein production

For pulldown assays using glutathione *S*-transferase fusions of the CDs of CDHR2 and CDHR5, the constructs were transformed into BL21(DE3) bacteria, expressed, and purified using GSH resin using standard conditions as previously described (8). For production of mNEON alone, mNEON–ANKS4B LK, and mNEON–Myo10 CC, the constructs were transformed into the *E. coli* strain DH5α, expressed, and purified using Ni–NTA–agarose (Qiagen) using standard conditions. Purifications were performed at 4 °C unless otherwise noted. The cells were harvested, resuspended in cold lysis buffer (50 mM $NaPO_4$, pH 8.0, 300 mM NaCl, 10 mM imidazole, 1 mg/ml lysozyme, 1 mM phenylmethylsulfonyl fluoride), lysed by sonication, and centrifuged at 15,000 × *g* for 1 h. The soluble lysate material was recovered and incubated with a 2-ml bed volume of pre-equilibrated Ni–NTA–agarose resin (Qiagen). The resins were incubated with cell lysates for 1 h on a rocking platform. The lysate–Ni–NTA mixture was then loaded into a column and subsequently washed with wash buffer (50 mM $NaPO_4$, pH 8.0, 300 mM NaCl, 20 mM imidazole) by gravity chromatography. Recombinant protein was eluted from the Ni–NTA resin using elution buffer (50 mM $NaPO_4$, pH 8.0, 300 mM NaCl, 250 mM imidazole). Eluates were analyzed by SDS-PAGE, and those fractions containing recombinant protein were pooled, and further purification steps were performed using an ÄKTA start protein purification system (GE Healthcare). Fractions containing recombinant protein were desalted using a HiTrap desalting column with an isocratic elution in 100 mM $NaPO_4$, pH 7.4 buffer. mNEON alone and mNEON–ANKS4B LK samples were pooled separately and loaded onto a HiTrap SP HP column (GE Healthcare) and eluted across a linear gradient from 0 to 1 M NaCl in 100 mM $NaPO_4$, pH 7.4. mNEON–Myo10 CC fractions were pooled and loaded on a HiTrap Q HP column (GE Healthcare) and eluted across a linear gradient from 0 to 1 M NaCl in 20 mM Tris-HCl, pH 7.5. Eluates were analyzed by SDS-PAGE, and those containing recombinant protein were pooled, loaded back onto Ni–NTA resin (Qiagen) to concentrate the sample, and eluted in 1-ml fractions with elution buffer (50 mM NaH_2PO_4, pH 8.0, 300 mM

NaCl, 250 mM imidazole). Eluates were then subjected to size-exclusion chromatography analysis using a HiPrep Sephacryl S-100HR column equilibrated in 100 mM $NaPO_4$, pH 7.4, 150 mM NaCl.

Microscopy

Cells and tissue sections were imaged using a Leica SP8 laser-scanning confocal microscope equipped with HyVolution deconvolution software. Paraffin-embedded intestinal tissue sections from mice were prepared as previously described (8). The samples were stained using anti-ANKS4B (1:200; Abnova catalog no. H00257629-M03), and anti-pERM (1:200; Cell Signaling catalog no. 3726) followed by Alexa Fluor 488 donkey anti-mouse (1:200; Invitrogen) and Alexa Fluor 568 donkey anti-rabbit (1:200; Invitrogen). CACO-2_{BBE} monolayers were washed once in warm PBS, incubated briefly with 0.02% saponin (Sigma) in warm PBS, and then fixed for 15 min with 4% paraformaldehyde in warm PBS containing 0.1% Triton X-100 (Sigma). After fixation, the cells were washed three times with warm PBS and blocked overnight in 5% BSA solution. Immunostaining was performed using anti-ANKS4B (1:200; Abnova catalog no. H00257629-M03), anti-CDHR2 (1:75; Sigma catalog no. HPA012569), anti-USH1C (1:70; Sigma catalog no. HPA027398), anti-Myo7b (1:25; Sigma catalog no. HPA039131), and anti-GFP (1:200; Aves laboratory catalog no. GFP1020) primary antibodies at 37 °C for 2 h. The coverslips were washed three times with warm PBS and incubated for 1 h with Alexa Fluor 488 donkey anti-rabbit, Alexa Fluor 488 donkey anti-mouse (1:200), and Alexa Fluor 488 goat anti-chicken (1:200) secondary antibodies (where appropriate) along with Alexa Fluor 568 phalloidin (1:200). The coverslips were then washed five times in PBS and mounted with Prolong Diamond anti-fade reagent (Invitrogen). All images shown are *en face* maximum projections through the full height of the BB, with the exception of the *x*–*z* sections, which are single plane confocal images. HeLa cells were washed once in warm PBS, fixed for 15 min with 4% paraformaldehyde in warm PBS, and then incubated with 0.1% Triton X-100 (Sigma) for 7 min. After fixation and permeabilization, the cells were washed three times with warm PBS and blocked overnight in a filtered 5% BSA solution. Staining was performed with Alexa Fluor 568 phalloidin (1:200) at 37 °C for 2 h. The coverslips were then washed five times in PBS and mounted with Prolong Diamond anti-fade reagent (Invitrogen). All images shown are *en face* maximum projections through the full height of the cells.

Image analysis

Image analysis was performed using ImageJ (National Institutes of Health). For line-scan signal analysis, a line was drawn through the BB oriented parallel to the microvillar axis as judged by either the F-actin signal. The intensity of the various channel signals along that line was subsequently recorded and normalized to the maximum grayscale value for an 8-bit image (*i.e.* 255). The corresponding positions for each intensity value was normalized so that the base of the microvillus was equal to 0 and the tip was equal to 1. Normalized line scans were then plotted together and fit to a single Gaussian using nonlinear regression (Prism version 6, GraphPad), which revealed the position of peak signal intensity and distribution width (S.D.) relative to the microvillar axis. For analysis of construct enrichment in microvilli, we calculated the ratio of BB to cytosolic signal intensity as previously described (8). The data were analyzed in a blinded fashion.

Analysis of microvillar clustering in CACO-2_{BBE} cells

The cells expressing either EGFP–ANKS4B LK or CDHR2–EGFP were allowed to polarize for 12-day after reaching confluency and were subsequently stained for F-actin and EGFP. Individual cells were scored according to whether they exhibited nonclustering microvilli (see cell in Fig. S3*A*, zoomed panel, for example) or robust microvillar clustering (*i.e.* possessing one or more distinct clusters of five or more microvilli; see asterisk-denoted cells in Fig. S3, *B* and *C*, zoomed panels). The cells were then scored for EGFP expression levels (low or high) as follows. Each EGFP-positive cell was outlined in ImageJ, and the ratio of the integrated relative fluorescence signal density to area was determined. The cells possessing a ratio 1–40 were assigned as low-expressing cells and greater than 40 as high-expressing cells.

Isolated BB binding assays

BBs were isolated from 21-day polarized CACO-2_{BBE} cells as previously described (11). For binding assays using recombinant mNEON-tagged proteins, BB material was first resuspended in 1 ml of blocking solution (20 mM imidazole, pH 7.2, 4 mM EDTA, 1 mM 4-(2-aminoethyl) benzenesulfonyl fluoride, 2.5% BSA, and 1 tablet of Roche protease inhibitor mixture per 10 ml of volume) for 30 min. Material was recovered by spinning at 3300 × *g* at 4 °C for 5 min in a cooling tabletop centrifuge. The recovered pellet was resuspended in BB blocking solution (500 μl) containing 100 μg of recombinant mNEON alone or mNEON–ANKS4B LK protein. The mixtures were incubated for 20 min on a rocking platform at 4 °C. The material was then recovered by spinning at 3300 × *g* at 4 °C for 5 min and washed 5 × 500 μl with blocking solution. After the final wash, material was recovered by spinning at 3300 × *g* at 4 °C for 5 min, and the mNEON signal was visualized using a blue light transilluminator.

Pulldown assays

For pairwise pulldown assays, HEK293T cells were grown in 10-cm dishes to 90% confluency and transfected using polyethylenimine reagent (Polysciences). After 48 h, the cells were washed once in warm PBS, recovered using a cell scraper, and lysed in ice-cold CelLytic M buffer (Sigma) containing 2 mM ATP, 1× cOmplete ULTRA protease inhibitor mixture (Roche), and 1 mM Pefabloc SC (Roche). The lysates were centrifuged at 16,000 × *g*, and the soluble fraction was recovered and incubated with a 50-μl bed volume of either pre-equilibrated anti-Flag M2 resin (Sigma) or GSH resin (Sigma) coupled with glutathione *S*-transferase fused to the CDs of the IMAC protocadherins. Resins were incubated with cell lysates for 2 h of rocking at 4 °C; pelleted by a low-speed spin; washed four times using radioimmune precipitation assay buffer supplemented with 2 mM ATP, 1× cOmplete ULTRA protease inhibitor mixture (Roche), and 1 mM Pefabloc SC (Roche); and eluted

ASBMB

by boiling in 2× SDS buffer to recover bound material. Resin-bound material was detected by either staining with Coomassie Blue or Western blotting analysis with the following antibody dilutions: mouse anti-Flag M2 (1:1000; Sigma catalog no. F3165) and mouse anti-GFP (1:1000; Santa Cruz catalog no. sc-9996). All pulldown assays were repeated at least three times in independent experiments, and the results shown are representative.

Statistical analysis

All graphs were generated and statistical analyses was performed using Prism v.6 (GraphPad). For all figures, the *error bars* represent standard deviations. Unpaired *t tests* were employed determine statistical significance between reported values.

Data availability

All the data are found within the article.

Acknowledgments—We thank all members of the Crawley laboratory for advice and support.

Author contributions—M. J. G., S. M., and S. W. C. data curation; M. J. G., S. M., and S. W. C. formal analysis; M. J. G., S. M., M. S. C., Z. A. S., R. A. E. S. I., B. K. P., P. A., P. E. S., T. O. A., and S. W. C. investigation; M. J. G., S. M., and S. W. C. writing-review and editing; S. W. C. conceptualization; S. W. C. supervision; S. W. C. funding acquisition; S. W. C. methodology; S. W. C. writing-original draft; S. W. C. project administration.

Funding and additional information—This work was supported by National Institutes of Health Grant R15GM131382 (to S. W. C.). This work was also supported by an Northern Ohio Alliances for Graduate Education and the Professoriate (NOA-AGEP) fellowship (to M. J. G.), First Year Summer Research Experience (FYSRE) and Undergraduate Summer Research and Creative Activities Program (USR-CAP) University of Toledo scholarships (to Z. A. S. and R. A. E. S. I.), and University of Toledo startup funds (to S. W. C.). The content is solely the responsibility of the authors and does not necessarily represent the official views of the National Institutes of Health.

Conflict of interest—The authors declare that they have no conflicts of interest with the contents of this article.

Abbreviations—The abbreviations used are: BB, brush border; IMAC, intermicrovillar adhesion complex; CEN, central unstructured region; SAM, sterile α-motif; PBM, PDZ-binding motif; KD, knockdown; USH1, type 1 Usher syndrome; aa, amino acid(s); ERM, Ezrin–Radixin–Merlin; LK, linker segment; CC, coiled-coil; SRP, serine-rich patch; BH, basic-hydrophobic; BHB, basic-hydrophobic-basic; Myo10 CC, CC motif of Myosin-10; CD, cytoplasmic domain; shRNA, short hairpin RNA; Ni–NTA, nickel–nitrilotriacetic acid.

References

1. Crawley, S. W., Mooseker, M. S., and Tyska, M. J. (2014) Shaping the intestinal brush border. *J. Cell Biol.* **207,** 441–451 CrossRef Medline
2. Pelaseyed, T., Bergström, J. H., Gustafsson, J. K., Ermund, A., Birchenough, G. M., Schütte, A., van der Post, S., Svensson, F., Rodríguez-Piñeiro, A. M., Nyström, E. E., Wising, C., Johansson, M. E., and Hansson, G. C. (2014) The mucus and mucins of the goblet cells and enterocytes provide the first defense line of the gastrointestinal tract and interact with the immune system. *Immunol. Rev.* **260,** 8–20 CrossRef Medline
3. Sun, W. W., Krystofiak, E. S., Leo-Macias, A., Cui, R., Sesso, A., Weigert, R., Ebrahim, S., and Kachar, B. (2020) Nanoarchitecture and dynamics of the mouse enteric glycocalyx examined by freeze-etching electron tomography and intravital microscopy. *Commun. Biol.* **3,** 5 CrossRef Medline
4. McConnell, R. E., Higginbotham, J. N., Shifrin, D. A., Jr., Tabb, D. L., Coffey, R. J., and Tyska, M. J. (2009) The enterocyte microvillus is a vesicle-generating organelle. *J. Cell Biol.* **185,** 1285–1298 CrossRef Medline
5. Shifrin, D. A., Jr., McConnell, R. E., Nambiar, R., Higginbotham, J. N., Coffey, R. J., and Tyska, M. J. (2012) Enterocyte microvillus-derived vesicles detoxify bacterial products and regulate epithelial-microbial interactions. *Curr. Biol.* **22,** 627–631 CrossRef Medline
6. Wilson, W., Scott, R. B., Pinto, A., and Robertson, M. A. (2001) Intractable diarrhea in a newborn infant: microvillous inclusion disease. *Can. J. Gastroenterol.* **15,** 61–64 CrossRef Medline
7. Vallance, B. A., Chan, C., Robertson, M. L., and Finlay, B. B. (2002) Enteropathogenic and enterohemorrhagic *Escherichia coli* infections: emerging themes in pathogenesis and prevention. *Can. J. Gastroenterol.* **16,** 771–778 CrossRef Medline
8. Crawley, S. W., Shifrin, D. A., Jr., Grega-Larson, N. E., McConnell, R. E., Benesh, A. E., Mao, S., Zheng, Y., Zheng, Q. Y., Nam, K. T., Millis, B. A., Kachar, B., and Tyska, M. J. (2014) Intestinal brush border assembly driven by protocadherin-based intermicrovillar adhesion. *Cell* **157,** 433–446 CrossRef Medline
9. Crawley, S. W., Weck, M. L., Grega-Larson, N. E., Shifrin, D. A., Jr., and Tyska, M. J. (2016) ANKS4B is essential for intermicrovillar adhesion complex formation. *Dev. Cell* **36,** 190–200 CrossRef Medline
10. Weck, M. L., Crawley, S. W., Stone, C. R., and Tyska, M. J. (2016) Myosin-7b promotes distal tip localization of the intermicrovillar adhesion complex. *Curr. Biol.* **26,** 2717–2728 CrossRef Medline
11. Choi, M. S., Graves, M. J., Matoo, S., Storad, Z. A., El Sheikh Idris, R. A., Weck, M. L., Smith, Z. B., Tyska, M. J., and Crawley, S. W. (2020) The small EF-hand protein CALML4 functions as a critical myosin light chain within the intermicrovillar adhesion complex. *J. Biol. Chem.* **295,** 9281–9296 CrossRef Medline
12. Yu, I. M., Planelles-Herrero, V. J., Sourigues, Y., Moussaoui, D., Sirkia, H., Kikuti, C., Stroebel, D., Titus, M. A., and Houdusse, A. (2017) Myosin 7 and its adaptors link cadherins to actin. *Nat. Commun.* **8,** 15864 CrossRef Medline
13. Li, J., He, Y., Lu, Q., and Zhang, M. (2016) Mechanistic basis of organization of the harmonin/USH1C-mediated brush border microvilli tip–link complex. *Dev Cell* **36,** 179–189 CrossRef Medline
14. He, Y., Li, J., and Zhang, M. (2019) Myosin VII, USH1C, and ANKS4B or USH1G together form condensed molecular assembly via liquid–liquid phase separation. *Cell Rep.* **29,** 974–986.e4 CrossRef Medline
15. Peterson, M. D., and Mooseker, M. S. (1993) An *in vitro* model for the analysis of intestinal brush border assembly: I. Ultrastructural analysis of cell contact-induced brush border assembly in Caco-2BBe cells. *J. Cell Sci.* **105,** 445–460 Medline
16. Johnston, A. M., Naselli, G., Niwa, H., Brodnicki, T., Harrison, L. C., and Góñez, L. J. (2004) Harp (harmonin-interacting, ankyrin repeat-containing protein), a novel protein that interacts with harmonin in epithelial tissues. *Genes Cells* **9,** 967–982 CrossRef Medline
17. Weil, D., El-Amraoui, A., Masmoudi, S., Mustapha, M., Kikkawa, Y., Lainé, S., Delmaghani, S., Adato, A., Nadifi, S., Zina, Z. B., Hamel, C., Gal, A., Ayadi, H., Yonekawa, H., and Petit, C. (2003) Usher syndrome type I G (USH1G) is caused by mutations in the gene encoding SANS, a protein that associates with the USH1C protein, harmonin. *Hum. Mol. Genet.* **12,** 463–471 CrossRef Medline
18. Pan, L., and Zhang, M. (2012) Structures of usher syndrome 1 proteins and their complexes. *Physiology (Bethesda)* **27,** 25–42 CrossRef Medline
19. Ahmed, Z. M., Riazuddin, S., Bernstein, S. L., Ahmed, Z., Khan, S., Griffith, A. J., Morell, R. J., Friedman, T. B., Riazuddin, S., and Wilcox, E. R. (2001)

Mutations of the protocadherin gene PCDH15 cause Usher syndrome type 1F. *Am. J. Hum. Genet.* **69,** 25–34 CrossRef Medline
20. Bitner-Glindzicz, M., Lindley, K. J., Rutland, P., Blaydon, D., Smith, V. V., Milla, P. J., Hussain, K., Furth-Lavi, J., Cosgrove, K. E., Shepherd, R. M., Barnes, P. D., O'Brien, R. E., Farndon, P. A., Sowden, J., Liu, X. Z., *et al.* (2000) A recessive contiguous gene deletion causing infantile hyperinsulinism, enteropathy and deafness identifies the Usher type 1C gene. *Nat. Genet.* **26,** 56–60 CrossRef Medline
21. Bolz, H., von Brederlow, B., Ramírez, A., Bryda, E. C., Kutsche, K., Nothwang, H. G., Seeliger, M., del, C. S. C. M., Vila, M. C., Molina, O. P., Gal, A., and Kubisch, C. (2001) Mutation of CDH23, encoding a new member of the cadherin gene family, causes Usher syndrome type 1D. *Nat. Genet.* **27,** 108–112 CrossRef Medline
22. Bork, J. M., Peters, L. M., Riazuddin, S., Bernstein, S. L., Ahmed, Z. M., Ness, S. L., Polomeno, R., Ramesh, A., Schloss, M., Srisailpathy, C. R., Wayne, S., Bellman, S., Desmukh, D., Ahmed, Z., Khan, S. N., *et al.* (2001) Usher syndrome 1D and nonsyndromic autosomal recessive deafness DFNB12 are caused by allelic mutations of the novel cadherin-like gene CDH23. *Am. J. Hum. Genet.* **68,** 26–37 CrossRef Medline
23. Verpy, E., Leibovici, M., Zwaenepoel, I., Liu, X. Z., Gal, A., Salem, N., Mansour, A., Blanchard, S., Kobayashi, I., Keats, B. J., Slim, R., and Petit, C. (2000) A defect in harmonin, a PDZ domain-containing protein expressed in the inner ear sensory hair cells, underlies Usher syndrome type 1C. *Nat. Genet.* **26,** 51–55 CrossRef Medline
24. Weil, D., Blanchard, S., Kaplan, J., Guilford, P., Gibson, F., Walsh, J., Mburu, P., Varela, A., Levilliers, J., and Weston, M. D. (1995) Defective myosin VIIA gene responsible for Usher syndrome type 1B. *Nature* **374,** 60–61 CrossRef Medline
25. Hussain, K., Bitner-Glindzicz, M., Blaydon, D., Lindley, K. J., Thompson, D. A., Kriss, T., Rajput, K., Ramadan, D. G., Al-Mazidi, Z., Cosgrove, K. E., Dunne, M. J., and Aynsley-Green, A. (2004) Infantile hyperinsulinism associated with enteropathy, deafness and renal tubulopathy: clinical manifestations of a syndrome caused by a contiguous gene deletion located on chromosome 11p. *J. Pediatr. Endocrinol. Metab.* **17,** 1613–1621 CrossRef Medline
26. Fehon, R. G., McClatchey, A. I., and Bretscher, A. (2010) Organizing the cell cortex: the role of ERM proteins. *Nat. Rev. Mol. Cell Biol.* **11,** 276–287 CrossRef Medline
27. Pataky, F., Pironkova, R., and Hudspeth, A. J. (2004) Radixin is a constituent of stereocilia in hair cells. *Proc. Natl. Acad. Sci. U.S.A.* **101,** 2601–2606 CrossRef Medline
28. Berryman, M., Franck, Z., and Bretscher, A. (1993) Ezrin is concentrated in the apical microvilli of a wide variety of epithelial cells whereas moesin is found primarily in endothelial cells. *J. Cell Sci.* **105,** 1025–1043 Medline
29. Pelaseyed, T., and Bretscher, A. (2018) Regulation of actin-based apical structures on epithelial cells. *J. Cell Sci.* **131,** jcs221853 CrossRef Medline
30. Sigrist, C. J. A., de Castro, E., Cerutti, L., Cuche, B. A., Hulo, N., Bridge, A., Bougueleret, L., and Xenarios, I. (2013) New and continuing developments at PROSITE. *Nucleic Acids Res.* **41,** E344–E347 Medline
31. McConnell, R. E., Benesh, A. E., Mao, S., Tabb, D. L., and Tyska, M. J. (2011) Proteomic analysis of the enterocyte brush border. *Am. J. Physiol. Gastrointest. Liver Physiol.* **300,** G914–G926 CrossRef Medline
32. Disanza, A., Carlier, M. F., Stradal, T. E., Didry, D., Frittoli, E., Confalonieri, S., Croce, A., Wehland, J., Di Fiore, P. P., and Scita, G. (2004) Eps8 controls actin-based motility by capping the barbed ends of actin filaments. *Nat. Cell Biol.* **6,** 1180–1188 CrossRef Medline
33. Brzeska, H., Guag, J., Remmert, K., Chacko, S., and Korn, E. D. (2010) An experimentally based computer search identifies unstructured membrane-binding sites in proteins: application to class I myosins, PAKS, and CARMIL. *J. Biol. Chem.* **285,** 5738–5747 CrossRef Medline
34. Shaner, N. C., Lambert, G. G., Chammas, A., Ni, Y., Cranfill, P. J., Baird, M. A., Sell, B. R., Allen, J. R., Day, R. N., Israelsson, M., Davidson, M. W., and Wang, J. (2013) A bright monomeric green fluorescent protein derived from *Branchiostoma lanceolatum*. *Nat. Methods* **10,** 407–409 CrossRef Medline
35. Lu, Q., Ye, F., Wei, Z., Wen, Z., and Zhang, M. (2012) Antiparallel coiled-coil-mediated dimerization of myosin X. *Proc. Natl. Acad. Sci. U.S.A.* **109,** 17388–17393 CrossRef Medline
36. Brzeska, H., Hwang, K. J., and Korn, E. D. (2008) Acanthamoeba myosin IC colocalizes with phosphatidylinositol 4,5-bisphosphate at the plasma membrane due to the high concentration of negative charge. *J. Biol. Chem.* **283,** 32014–32023 CrossRef Medline
37. Brzeska, H., Gonzalez, J., Korn, E. D., and Titus, M. A. (2020) Basic-hydrophobic sites are localized in conserved positions inside and outside of PH domains and affect localization of *Dictyostelium myosin* 1s. *Mol. Biol. Cell* **31,** 101–117 CrossRef Medline
38. Mazerik, J. N., and Tyska, M. J. (2012) Myosin-1A targets to microvilli using multiple membrane binding motifs in the tail homology 1 (TH1) domain. *J. Biol. Chem.* **287,** 13104–13115 CrossRef Medline
39. Tyska, M. J., Mackey, A. T., Huang, J. D., Copeland, N. G., Jenkins, N. A., and Mooseker, M. S. (2005) Myosin-1a is critical for normal brush border structure and composition. *Mol. Biol. Cell* **16,** 2443–2457 CrossRef Medline
40. Overlack, N., Kilic, D., Bauss, K., Märker, T., Kremer, H., van Wijk, E., and Wolfrum, U. (2011) Direct interaction of the Usher syndrome 1G protein SANS and myomegalin in the retina. *Biochim. Biophys. Acta* **1813,** 1883–1892 CrossRef Medline
41. Bauë, K., Knapp, B., Jores, P., Roepman, R., Kremer, H., Wijk, E. V., Märker, T., and Wolfrum, U. (2014) Phosphorylation of the Usher syndrome 1G protein SANS controls Magi2-mediated endocytosis. *Hum. Mol. Genet.* **23,** 3923–3942 CrossRef Medline
42. Sorusch, N., Yildirim, A., Knapp, B., Janson, J., Fleck, W., Scharf, C., and Wolfrum, U. (2019) SANS (USH1G) molecularly links the human Usher syndrome protein network to the intraflagellar transport module by direct binding to IFT-B proteins. *Front. Cell Dev. Biol.* **7,** 216 CrossRef Medline
43. Adato, A., Michel, V., Kikkawa, Y., Reiners, J., Alagramam, K. N., Weil, D., Yonekawa, H., Wolfrum, U., El-Amraoui, A., and Petit, C. (2005) Interactions in the network of Usher syndrome type 1 proteins. *Hum. Mol. Genet.* **14,** 347–356 CrossRef Medline
44. Sorusch, N., Bauë, K., Plutniok, J., Samanta, A., Knapp, B., Nagel-Wolfrum, K., and Wolfrum, U. (2017) Characterization of the ternary Usher syndrome SANS/ush2a/whirlin protein complex. *Hum. Mol. Genet.* **26,** 1157–1172 CrossRef Medline
45. Boëda, B., El-Amraoui, A., Bahloul, A., Goodyear, R., Daviet, L., Blanchard, S., Perfettini, I., Fath, K. R., Shorte, S., Reiners, J., Houdusse, A., Legrain, P., Wolfrum, U., Richardson, G., and Petit, C. (2002) Myosin VIIa, harmonin and cadherin 23, three Usher I gene products that cooperate to shape the sensory hair cell bundle. *EMBO J.* **21,** 6689–6699 CrossRef Medline
46. Bahloul, A., Pepermans, E., Raynal, B., Wolff, N., Cordier, F., England, P., Nouaille, S., Baron, B., El-Amraoui, A., Hardelin, J. P., Durand, D., and Petit, C. (2017) Conformational switch of harmonin, a submembrane scaffold protein of the hair cell mechanoelectrical transduction machinery. *FEBS Lett.* **591,** 2299–2310 CrossRef Medline
47. Meerbrey, K. L., Hu, G., Kessler, J. D., Roarty, K., Li, M. Z., Fang, J. E., Herschkowitz, J. I., Burrows, A. E., Ciccia, A., Sun, T., Schmitt, E. M., Bernardi, R. J., Fu, X., Bland, C. S., Cooper, T. A., Schiff, R., Rosen, J. M., Westbrook, T. F., and Elledge, S. J. (2011) The pINDUCER lentiviral toolkit for inducible RNA interference in vitro and in vivo. *Proc Natl Acad Sci U S A* **108,** 3665–3670 CrossRef Medline.

ASBMB